PERGAMON

International Journal of Solids and Structures 40 (2003) 6723–6765

INTERNATIONAL JOURNAL OF SOLIDS and STRUCTURES

www.elsevier.com/locate/ijsolstr

A new membrane model for the ballistic impact response and V_{50} performance of multi-ply fibrous systems

S. Leigh Phoenix *, Pankaj K. Porwal

Department of Theoretical and Applied Mechanics, Cornell University, 321 Thurston Hall, Ithaca, NY 14853, USA

Received 18 January 2003; received in revised form 6 June 2003

Abstract

This paper develops an analytical model for the ballistic impact response of fibrous materials of interest in body armor applications. It focuses on an un-tensioned 2D membrane impacted transversely by a blunt-nosed projectile, a problem that has remained unsolved for a half a century. Membrane properties are assumed characteristic of the best current body armor materials (Kevlar®, Spectra®, Zylon®, S2 glass), which have very high stiffness and strength per unit weight, and low strain-to-failure. Successful comparisons will be made with extensive experimental data on such material systems as reported by Cunniff [Decoupled response of textile body armor. Proc. 18th Int. Symp. of Ballistics, San Antonio, Texas, 1999a, pp. 814–821; V_s–V_r relationships in textile system impact. Proc. 18th Int. Symp. of Ballistics, San Antonio, Texas, 1999b; Dimensional parameters for optimization of textile-based body armor systems, Proc. 18th Int. Symp. of Ballistics, San Antonio, Texas, 1999c, pp. 1303–1310]. Our mathematical formulation draws on the seminal work of Rakhmatulin and Dem'yanov [Strength Under High Transient Loads, 1961, pp. 94–152]. Under constant projectile velocity we first develop self-similar solution forms for the tensile 'implosion' wave and the curved cone wave that develops in its wake. Through matching boundary conditions at the cone wave front, we obtain an accurate approximate solution for the membrane response including cone wave speed and strain distribution. We then consider projectile deceleration due to membrane reactive forces, and obtain results on cone velocity, displacement and strain concentration versus time. Other results obtained are the membrane ballistic limit, or V_{50} velocity, and the residual velocity when penetrated above this limit. We then derive an exact functional representation of a V_{50} 'master curve' found empirically by Cunniff [ibid] to reduce data for a wide variety of fabric systems impacted by blunt cylindrical projectiles. This curve is given in terms two dimensionless parameters based only on fiber mechanical properties and the ratio of the fabric areal density to the projectile mass divided by its area of fabric contact. Our functional representation has no fitting parameters beyond one reflecting uncertainty in the effective diameter of the impact zone relative to the projectile diameter, and even then the values are consistent across several experimental systems. The extremely successful comparison of our analytical model to experimental results in the literature raises fundamental questions about many long-held views on fabric system impact behavior and parameters thought to be important.

Keywords: Fabric ballistic impact; Body armor; V_{50} performance

* Corresponding author. Tel.: +1-607-255-8818; fax: +1-607-255-2011.
E-mail address: slp6@cornell.edu (S. Leigh Phoenix).

0020-7683/$ - see front matter © 2003 Elsevier Ltd. All rights reserved.
doi:10.1016/S0020-7683(03)00329-9

1. Introduction

The development of lightweight fibrous material systems to resist penetration by high-velocity bullets has been an important research topic since World War II and even moreso since the terrorist attacks of September 11, 2001. The most effective body armor for military and law enforcement personnel involves multi-ply fabrics and flexible fibrous composites sometimes placed behind a hard ceramic strike face (e.g., 5–10 mm of B_4C) to blunt armor-piercing rounds. These fibrous materials are also key components in armor panels for automobiles, light military vehicles, helicopters and airline cockpit doors.

The last few decades have indeed seen the development of greatly improved fibrous materials for ballistic protection. Nylon fibers were dominant prior to 1972, and these showed considerable non-linearity in stress–strain response, with relatively high strains to failure. In the decades since, new polymeric fibrous materials have been developed that exhibit greatly improved performance. They include aramids (e.g., Kevlar®, Twaron®, Technora®) highly oriented polyethylene (e.g., Spectra®, Dyneema®) and PBO (e.g. Zylon®), and more such as PIPD (M5®) are being developed. In tension, all these materials differ greatly from their nylon predecessors, having very high stiffness, extremely high strength to weight ratios, and very low strains to failure (<4%). They are essentially elastic in tension, both at low and high rates of loading, where stiffness differences are minor. At the same time, they are similar to nylon in transverse compression, undergoing large plastic deformation without a significant reduction in tensile load-carrying ability (unlike carbon or glass fibers, which shatter). The best of these, PBO, has a tensile strength of 5.2 GPa, more than three times the strength of the strongest steel (piano wire) at 1/5 the density; their strength to weight advantage is *fifteen*.

To provide perspective, Fig. 1 illustrates a sequence of possible events that a futuristic, lightweight material system (perhaps 40% the weight of current systems) might undergo to halt an armor-piercing bullet. Such 10 g bullets have a tool steel core (grey) a lead nose (black) and a gliding metal surface (copper color). In present armor systems, bullet blunting is provided by a 5 – 10 mm hard ceramic surface (e.g., B_4C) and the bullet deformation sequence shown in Fig. 1 reflects observations from X-ray experiments (Anderson and Gooch, 2001). In our hypothetical system, however, the much thinner, ultra-hard surface, eventually moves with the blunted bullet, whereas in current body armor, the ceramic is finally penetrated, passing the blunted bullet and ceramic debris to a fibrous composite layer beneath (e.g., Spectra Shield® or

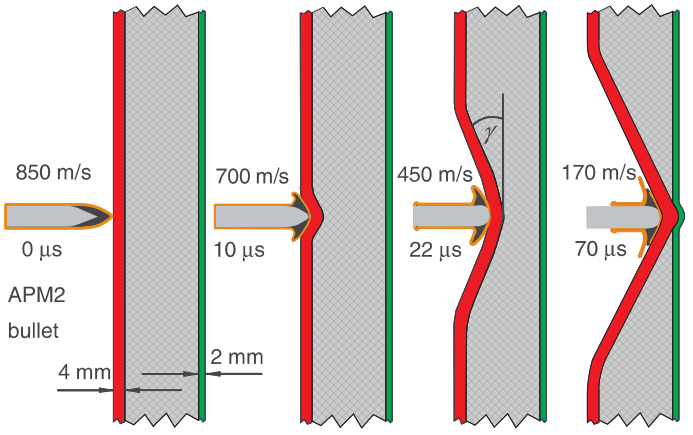

Fig. 1. Schematic of a hypothetical layered fibrous structure envisioned to stop armor piercing APM2 bullets, yet half the weight of current, state-of-the art systems. What structural analysis and material properties would be necessary to achieve such a revolutionary structure?

S2 glass). Integral with the hard strike face might be a functionally graded, fibrous material, a few mm thick that develops an impact wave as a growing cone. The bullet may be slowed enough over the next 1–2 cm to be stopped finally by a third, soft layer (e.g., plies of Kevlar® KM2 fabric).

Questions arise from the fictitious description depicted in Fig. 1: Is such a lightweight armor system possible, given foreseeable advances in nanotechnology? Is the sequence of events described physically realistic for the armor weight assumed? What might be the ideal armor architecture and design? Should it be a 'rigid' composite or be flexible with unbonded layers and little or no matrix? Would a three-dimensional weave be superior to multiple layers of two-dimensional (2D) fabric of the same thickness? The goal of this paper is to develop a model that would go a long way towards making such an assessment possible.

To understand the impact response of such fibrous systems, one must first consider the basic building blocks: single-ply fabrics, and single yarns and fibers. Their response to high velocity impact is difficult to model because it differs from the common experience of a drum struck with a mallet, or a guitar string struck with a pic. These are under high initial tension that is not altered during wave motion, and transverse displacements and angles are small. Their modeling is amenable to classic mathematical techniques of linear vibrations, as treated in books on wave motion (e.g., Graff, 1991). The same is not true for the fibrous systems above; what complicates the analysis is that the impact velocities are large enough to drastically alter the tension (initially negligible in most cases) and the displacements and deflection angles are large.

Because of these mathematical complications, except for the little known monograph of Rakhmatulin and Dem'yanov (1961), ballistic impact on fibers, yarns and membranes is not treated in books. Nonetheless many theoretical papers have appeared on projectile impact into one-dimensional (1D) fibers and yarns, particularly from 1940 to the 1974. However, a comparable theoretical literature on 2D membranes is largely absent. To fill this theoretical vacuum, finite-element, simulation models of fabric impact began to appear in the 1970s, and although shedding some light on experiments, have not resulted in useful scaling relationships to guide body armor design. The simulations have also remained limited in system sizes and have suffered other difficulties discussed later. Thus, most research has necessarily involved costly and time-consuming trial-and-error experimentation.

Most of the theoretical literature was developed in the era of nylon and metals prior to 1970, and understandably emphasizes complexities due to non-linear tensile behavior, with much emphasis on plastic-like material characteristics. While leading to rich and diverse mathematical results, such emphasis has obscured understanding of simpler, elastic behavior typical of all the best current materials. In many early papers, elastic results are often left for the reader to extract from a complex non-linear analysis. Preoccupation with material non-linearities persists. Projectiles have enormous kinetic energy, and one way or another, this energy must be absorbed if they are to be stopped. For many researchers, this naked truth impulsively prompts thinking in terms of various measures of toughness, such as ductility, fracture toughness, frictional slip and even energy absorbed in phase transitions. As we shall see, such concepts are not necessary to explain the superiority of current fibrous materials in body armor.

The purpose of the present paper is to revisit the longstanding problem of blunt projectile impact on a 2D membrane, and to develop a new theory that yields accurate, closed-form approximations. These results will briefly be compared to experimental data in the literature on both single and multi-ply fabric structures. We begin, with a brief review of literature relevant to the current study.

1.1. Overview of literature on transverse impact of 1D string-like structures

The earliest work appears to be due to Taylor (1942). Following von Karmann (1942), Taylor treated the case of a plastic wave traveling down a wire extended by transverse impact. Broad fundamental advances, however, were due to Rakhmatulin (1945, 1947, 1951, 1952) and are summarized in the monograph of Rakhmatulin and Dem'yanov (1961), which also discusses works of Zverev (1949), Grigor'ev (1949), Ryabova (1953), Cristescu (1954) and Moroz (1956). In literature in English, Cole et al. (1953) are often

credited as having obtained the first major results, followed by the more general formulation of Craggs (1954) using the method of characteristics. However, many of the results in Cole et al. had appeared earlier in the work of Rakhmatulin (1945). Interestingly, Ringleb (1957) mentions a result in his 1948 US Government report relating the strain in an aircraft carrier arrest cable to the transverse impact velocity and longitudinal wave speed. His result became subject to military classification, but this was abandoned once it was discovered in the open literature (e.g., in Rakhmatulin (1945)).

In the US, papers on fibrous body armor development typically begin with reference to the work of Smith et al. (1958), which deals with transversely impacted yarns having non-linear, stress–strain curves characteristic of nylon. Their paper presents an elaborate treatment of the resulting complications in shock formation and wave speeds. Smith et al. (1960, 1963) summarize these results (and those of Cole et al. (1953)), and give explicit results for linear elastic behavior. They also treat interference effects from waves reflected from boundaries, which are used to interpret experiments on determining strain wave velocities. Many of these topics were also treated earlier in the Russian literature mentioned above, with similar results. Apparently the US authors were unaware of those works. The Russian works prior to 1958 are rarely referenced in literature in English.

Other work is that of Roylance (1973), who treated the effects of yarn linear viscoelasticity using a finite-element simulation, and Morrison (1984) who studied transverse impact on aramid yarns, both through experiments and finite-element simulations. Prevorsek et al. (1991) studied impact on high stiffness polyethylene yarns (Spectra®) and reported a doubling of the stiffness of Spectra® at ballistic loading rates.

Results on 1D problems have shed only modest light on behavior seen in 2D fabrics systems. Experiments show that their ballistic responses are very different in important ways. One reason is that results from 1D models are largely insensitive to the dimensions of the projectile tip, whereas experiments show these dimensions to be crucial in 2D fabric systems.

There also remains the issue of gleaning results from past analyses that are relevant to modeling the best current systems and guiding future research. In the past, new materials have been discovered largely by accident, and only after commercialization, mainly for other purposes, have they been found to be superior in ballistic protection. Recently, the US Government has committed substantial resources to developing new materials using advances in nanotechnology. The success of such efforts is likely to require much greater understanding of why current systems are so successful and what new directions might be ventured to yield even better performance. Otherwise such efforts risk failure. We believe that theoretical modeling and analysis has a key role to play in this process.

1.2. Overview of analytical literature on transverse impact of 2D membranes and fabrics

The earliest work on transverse impact of a projectile into an elastic membrane appears to be that of Grigoryan (1949) for point impact and neglecting circumferential (hoop) stresses. As mentioned in Rakhmatulin and Dem'yanov (1961) and shown in Galin (1949), neglecting circumferential stresses for point impact leads to unreasonable results. Rakhmatulin and Dem'yanov (1961) reformulated the governing partial differential equations to include circumferential stresses and Poisson's ratio effects, and presented very limited analytical results based on the work of Pavlenko (1952). These results were for the specialized case of impact by a sharply pointed cone under certain assumptions on projectile contact and interface slippage. While some insight can be gleaned, particularly with respect to solution approach and wave characteristics, the results provide little insight into membrane response under the more realistic case of impact by a blunt projectile (either blunted in the initial impact as with a lead bullet or first blunted by a sacrificial ceramic layer for harder bullets) where the nose diameter becomes a characteristic length scale.

The above authors concluded that circumferential hoop stresses are essential to a solution, but this conclusion is questionable in cases other than idealized point impact, where hoop stresses appear necessary to compensate for local singular behavior. For instance, singular behavior does not occur in models of

point impact on a 1D string. In fact, hoop strains in a membrane are typically negative and one cannot expect membranes and fabrics to support significant compressive stresses in plane without locally buckling. Including them, however, leads to overwhelming mathematical difficulties that led Rakhmatulin and Dem'yanov (1961) to express pessimism on the prospects for obtaining solutions using classical mathematical techniques. Another issue apparently little appreciated, is the subtle process of generating self-similar solutions for membrane deformation to obtain useful results. Mishandling of this aspect can lead to predicted excessive stresses upon impact that suggest premature membrane failure irrespective of velocity. In this respect, analysis for the 1D problem proves subtly misleading. The practically important aspect of having a length scale for the projectile tip, also drives the mathematical formulation, and without it the results lose relevance—if achievable at all.

Some approximate models of fabric impact have been published. Vinson and Zukas (1975) adapted a static conical shell theory to fabric impact by a blunt cylindrical projectile, thus introducing a key length scale. The model did not yield a wave speed for the deformation cone, so their numerical solution used experimental values in Maheux (1957). Their model results were compared to his nylon fabric experiments as well as those in Roylance et al. (1973), and one interesting result was a linear relationship between the maximum shell strain at penetration and the projectile striking velocity. Vinson and Walker (1997) used the same conical shell model to interpret experiments of Lee and Sun (1993) on impact into much more rigid graphite/epoxy laminates. They used the composite shear wave velocity as the cone edge wave speed and commented that the membrane strain energy dominates the bending strain energy to the point where the latter can be neglected, thus justifying the use of the conical shell model. They also comment that the matrix does not increase the resistance to ballistic penetration, a conclusion largely supported in other work discussed later. A linear relationship was again calculated between the maximum shell strain at penetration and the projectile striking velocity.

Walker (1999, 2001) developed an impact model for fabrics and flexible composites using a static deflection analysis for biaxial membranes under point loading and restrained edges. The model yielded a curved pyramid shape for fabric deflection including an expression for the pyramid edge wave speed. To obtain a relationship between the ballistic limit velocity and material parameters, Walker introduced a projectile nose radius, and the resulting function fit experimental data well. An unrealistic aspect was omission of in-plane material displacements towards the origin, as expected from tensile wave propagation. This resulted in unrealistically small pyramid angles at failure. We also mention modeling efforts by Scott (1999) who adapted a plate analysis to model the penetration of compliant composites, and Chocron-Benloulo et al. (1997) who extended the 1D yarn impact model by adding a strain energy based, damage variable. Cheeseman and Bogetti (2003) summarize recent thinking on fabric system impact.

1.3. Overview of literature on numerical simulation of impact on biaxial fabric systems

Mathematical difficulties in modeling membrane impact have prompted the development of numerical simulation models. The earliest efforts were those of Roylance et al. (1973) on biaxial fabrics. They implemented a dynamic form of finite-element analysis described in Mehta and Davids (1966), and obtained many behavioral features seen in experiments. One important feature, not occurring in 1D models, was strain intensification over time near the projectile impact point. This strain increase was attributed to the discrete nature of fabrics in terms of tensile wavelet reflections and interactions at yarn crossovers, said to cause attenuation at the strain wave front. This aspect was considered more by Roylance and Wang (1980). They found that energy conservation discrepancies in the projectile to fabric energy exchange were minimized upon taking the fabric tensile wave velocity to be that for the yarn divided by $\sqrt{2}$, a result one might expect as crossing yarns double the effective yarn mass without adding stiffness in the direction of wave propagation.

The simulation model of Roylance and coworkers has continued to evolve. A few results appeared in an overview article of Cunniff (1992), and further extensions appeared in Ting et al. (1993), and Roylance et al. (1995), where yarn slippage and wave interference were modeled in multi-ply fabric systems. Most recently, Cunniff and Ting (1999) introduced more detail on the out-of-plane yarn undulations with inter-yarn elastic couplings at crossovers, as well as subdivision of yarn segments between crossovers to increase resolution near the impact zone.

Other simulation models have appeared, such as the one of Johnson et al. (1999) whose finite-element model uses both bar and shell elements. This more general model permits a wider variety of target and projectile configurations and of material systems than those above, including the possibility of sliding of the projectile on the fabric. The model appeared to produce some results for residual velocity versus impact velocity consistent with experiments on multi-ply fabrics using RCC projectiles of various weights. However, the entire thickness of the multi-ply fabric was represented by a single layer of bar and shell elements, thus eliminating compliance through the thickness. Results were presented for Kevlar® KM2/polyethylene matrix composite targets showing membrane like behavior quite similar to that of the matrix free fabric systems, thus tending to support the contention of Vinson and Walker (1997).

Additional studies include Shim et al. (1995) using an orthogonal grid of pin-jointed, finite-elements, including effects of viscosity and crimp of orthogonal yarns. Simons et al. (2001) developed a finite-element model with applications to fragment containment in turbine failures, but the projectile velocities were an order of magnitude less than in other studies above. Prevorsek et al. (1991) developed a finite-element model for impact on Spectra® composites, including partial penetration with severe projectile deformation. Keefe et al. (2002) is developing a simulation model that shows considerable realism at capturing local details of fabric impact, as does the finite-element model of Lim et al. (2003), which also treats viscoelastic behavior.

Though useful, the simulation models above have suffered from various shortcomings. First, the models are susceptible to numerical 'ringing' oscillations attributable to the discrete elastic nature of the hinged lattice model, and the peak amplitudes can greatly exceed local average values. Given the emphasis placed by Roylance and coworkers on the role of discrete wavelet reflections, it then becomes difficult to argue that the oscillations are artifacts rather than critical features. Attempts at greater resolution in Cunniff and Ting (1999) seem to cause higher amplitude spikes and oscillation frequencies, thus exacerbating the ringing problem to the extent that some form of strain and displacement smoothing seems necessary, which defeats the purpose of the refinements. One method to control ringing has been to artificially add viscous damping as in Roylance and Wang (1980) and Johnson et al. (1999) and to apply some form of response smoothing. The latter authors, who did both, expressed concern that such additions are artificial and without physical basis. It also confounds accounting of projectile to fabric energy transfer and its redistribution in terms of elastic strain energy versus in-plane and out-of-plane kinetic energy. In a real system there is considerable heat generation, and undamped, pin-jointed fabric models reveal this thermal energy in terms of high-frequency ringing and associated strain spikes. Ironically, continuum models may have certain advantages in avoiding such problems.

A second shortcoming of most simulation results is a lack of attention paid to the projectile geometry and the size scale of the contact zone as key influences in fabric response. Although mentioned as model capabilities, reported results primarily assume projectile contact at a single point where two yarns cross. The key length scale de facto becomes the fabric yarn spacing rather than a projectile nose dimension, which is an important quantity in standardized fabric impact experiments. Furthermore, the initial stages of blunt impact become poorly modeled because of the initial pointed deflection at the impact node and the resulting strain concentration whose interpretation becomes unclear. As will be seen, these aspects are crucial to determining the strain concentration in the fabric adjacent to the projectile as well as initial momentum transfer, fabric energy distribution and potential local heat generation from impact. In the one instance where the projectile shape was modeled as a sphere versus a blunt cylinder by Johnson et al. (1999), large amounts of viscous damping and numerical smoothing were necessary to control the ringing. Such

difficulties may have become a deterrent in other studies as well, thus explaining the lack of results reporting effects of projectile shape and scale.

A third shortcoming of such simulation models is that computational demands rapidly escalate as larger systems are treated and more microstructural features are incorporated, often with conflicting results. Thus, while simulation models have great potential and have provided insight, consistent quantitative predictions have been elusive. Given the large number of microstructural parameters of potential significance in fabric impact response, some guidance of theory is essential to winnowing down this number to those most important.

1.4. Brief overview of literature on experimental studies of ballistic impact in fabrics

There exists a vast literature and data base from experimental studies of ballistic impact into fabric and flexible composite systems. This data base continues to grow through applying test standards such as NIJ Standard-0101.04, Revision A (2001) on new body armor systems. Much of the accessible data reflects various uncertainties since values for key parameters have been omitted (and even disguised for national security reasons). This hampers comparisons with model predictions. Nonetheless, sufficient data exists in reduced form to draw important conclusions. We make no attempt at a comprehensive review but will discuss certain results and frameworks often used to evaluate body armor systems.

Among the early works cited are those of Maheux (1957) on multi-ply armor panels and Wilde et al. (1973, 1974) on a photographic study of impact into nylon fabrics. These works give some details on retarding forces, energy absorption and deformation cone growth including its edge wave speed. Projectile geometry effects on fabric energy absorption were considered by Montgomery (1980). In developing a more efficient method for continuous-time measurement of projectile velocity and force, using a laser sheet system, Starratt et al. (1999, 2000) presented useful profiles for 8-ply Kevlar® 129 fabric systems impacted by blunt-tipped aluminum cylinders.

A commonly investigated theme is the relationship between the striking projectile velocity and the residual (exit) velocity after penetration. Prosser (1988) presented extensive results supporting his contention that, for a given multi-ply fabric system and projectile type, the energy absorbed during penetration is a constant, which is linearly dependent on the number of layers. This was believed to indicate that identical layers perform largely in a decoupled fashion, a theme pursued later in Cunniff (1999a). This same striking versus exit velocity relationship is further developed in Cunniff (1996, 1999b), who used a semi-empirical model with many regression coefficients to resolve impact data for various projectile types and angles of obliquity into various systems. Fabric layer decoupling and other system effects were discussed in Cunniff (1992) where anomalous coupling effects resulted from interchanging the order of Spectra® and Kevlar® fabrics plies having markedly different mechanical properties.

Finally we mention some remarkable results of Cunniff (1999c) who used a special pair of dimensionless parameters to reduce to one master curve V_{50} data for a wide variety of multi-ply fabric systems impacted by standardized cylindrical projectiles of unit aspect ratio and various masses. The materials were various deniers of Kevlar® 29 and KM2, Spectra 1000, PBO, and nylon, and the normalization required only the fiber elastic mechanical properties and density, and the ratio of the areal density of the fabric system to the mass of the RCC projectile divided by its cross-sectional area. These results will be crucial to our model verification.

1.5. Brief overview of the paper

In the present work we show that more complete solutions are indeed possible for important cases of 2D membrane impact, and that difficulties encountered previously stem from overlooking certain key transient solutions for the radially propagating tension waves. We obtain specific results for cases where elastic

membranes have low density, are stiff in tension, have very high strength and low strain to failure. These are precisely the properties of fibrous materials that presently yield the best performance per unit weight in body armor. We will also develop relevant results for impact into 1D systems (yarns, tapes) for purposes of comparison.

In Section 2 we formulate the partial differential equations for the 2D problem of an untensioned, elastic membrane impacted transversely by an axisymmetric, flat nosed projectile traveling at fixed velocity. The formulation follows that of Rakhmatulin and Dem'yanov (1961) where we neglect compressive hoop stresses since they are not supported in thin membranes. In Section 3 we give an accurate approximate solution to these equations based on the assumption of small meridional and radial membrane strains and generalized, self-similar scaling. Key to the solution is the length scale introduced by the radius of the flat projectile nose, and it is shown that the initial behavior is governed by the 1D solution, followed immediately by a sharp but continuous transition to characteristic 2D behavior as seen in experiments.

In Section 4, we adapt these results to model projectile deceleration due to reaction forces from the membrane. This deceleration has two regimes: first is sudden momentum transfer from blunt inelastic impact, and second is more gradual deceleration due to smooth energy transfer into the fabric in terms of kinetic energy and stored elastic energy. The analytical results obtained allow us to develop insight into various aspects of the impact event, such strain history in the fabric, evolution of the impact cone radius and its deflection by the projectile over time, including the distance needed to stop the projectile. Other results are the "V_{50}" velocity at the threshold for perforation and exit or residual velocity, V_{res}, after perforation at velocities above this threshold. Key scalings are revealed in terms of naturally arising dimensionless variables, and most of the results are explicit and require no numerical solution.

In Section 5, we use these results to model the response of a biaxial fabric system under transverse impact. We theoretically justify a dimensionless variable framework developed by Cunniff (1999b) to reduce V_{50} data for diverse fabric systems onto one "master curve". We obtain an explicit functional form, valid for all fabric to projectile areal density ratios. Our form additionally shows very minor dependence on the fabric failure strain. This functional form explicitly captures the strain concentration that develops in the fabric adjacent to the projectile, especially at lower areal density ratios. This feature is not approachable using 1D models.

In Section 6, we discuss the results on stress concentration and cone growth behavior, and briefly compare the predictions of the model to various experimental results in the literature. We obtain startlingly strong agreement despite only one adjustable parameter beyond fiber property values set already in the source literature. This parameter, which adjusts effective projectile diameter, is surprisingly constant across material systems. We also briefly discuss issues of momentum transfer, heat generation and rounded projectile tips. Section 7 presents some conclusions on further implications of the model with respect to misconceptions in the literature.

2. Assumptions and formulation of the 2D membrane impact problem

We consider the deformation over time $t > 0$ of a thin membrane due to impact by a right circular cylinder at time $t = 0$. This flat-nosed projectile with cylinder radius r_{p} and diameter $D_{\mathrm{p}} = 2r_{\mathrm{p}}$, and mass M_{p} travels at velocity V_{p} perpendicular to the membrane, and contact occurs over an area $A_{\mathrm{p}} = \pi r_{\mathrm{p}}^2 = \pi D_{\mathrm{p}}^2/4$. The membrane is initially untensioned and of infinite extent, and has quasi-isotropic, linearly elastic properties in plane. Its tensile modulus is E, Poisson's ratio is v, thickness is h, and density is ρ per unit volume. Because the tensile stresses are very large and the membrane is viewed as thin and fibrous, we neglect any compressive hoop stresses and associated Poisson effects since the fibers and yarns will locally buckle to relieve them. Fig. 2 illustrates some aspects of the geometry.

Modern ballistic fabrics to which the theory applies have a very low failure strain, ($\varepsilon_{\max} \leqslant 0.05$), high tensile stiffness ($E > 50$ GPa) and low density ($\rho < 2$ g/cm^2). Thus they have a very high tensile wave speed,

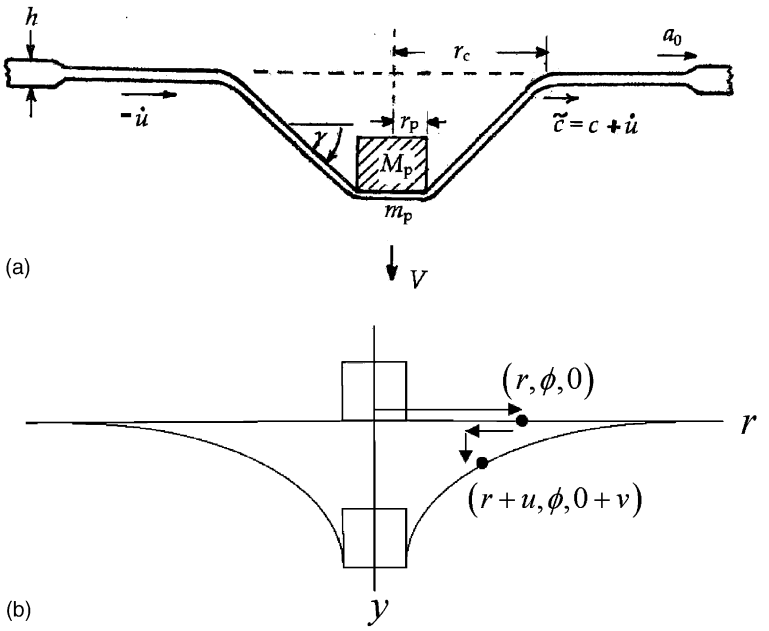

Fig. 2. Illustration of variables and geometry of the membrane impact problem: (a) the flow of membrane material towards the impact at velocity $\dot{u}$ lowers the cone edge wave speed, $\tilde{c}$, in ground coordinates compared to the value, c, in material (Lagrangian) coordinates. This material flow also allows large cone angles, γ. (b) Illustration of the cylindrical coordinate system (r, ϕ, y) and displacements (u, v). In a 2D membrane the cone shape has curvature as in (b).

which is an order of magnitude larger than projectile velocities of interest or the transverse wave speed of the growing deformation cone from impact. This allows us to make important simplifications in the projectile deceleration analysis.

In our first analysis we assume the projectile velocity V_p remains constant in time. A strain concentration rapidly develops in the membrane near the projectile, so the regime after impact over which the base of the impact cone grows a few projectile diameters in size is practically important. Our solution involves the development of several self-similar solution forms that combine to yield an accurate and insightful description of the behavior experimentally seen. We then extend the analysis to a decelerating projectile due to reactive forces from the membrane. A strain concentration develops but reaches a maximum and subsequently decays depending on the ratio of the fabric mass to the projectile mass in the area of first contact.

Expressing pessimism, Rakhmatulin and Dem'yanov (1961) claimed that neglecting hoop stresses to simplify the analysis leads to unrealistic and indeed "absurd" results. This is a misdiagnosis that is largely the result of overlooking the importance of a special self-similar solution for the initial formation of the expanding tensile wave in the fabric plane. This solution allows a crucial strain jump at the outward radiating tensile wave front as occurs in easier 1D analysis. Without it, instantaneous membrane failure and perforation is predicted no matter how small the projectile velocity, V_p, which Rakhmatulin and Dem'yanov (1961) rejected. We find that whether or not hoop stresses are neglected is irrelevant.

2.1. Fundamental partial differential equations under constant projectile velocity

We assume axisymmetric deformation of the membrane, and work with cylindrical coordinates (r, ϕ, y) shown in Fig. 2(b). At time $t = 0$ we let r and ϕ be the initial radial and circumferential location of a fabric

point in the infinite, untensioned membrane lying at rest in the level ground plane $y = 0$. A time t after impact, we let u and v be the in-plane and normal, out-of-plane components, respectively, of the displacement of this point, but its cylindrical angle ϕ remains the same. The new coordinates of the fabric point now become $(r + u, \phi, 0 + v)$ as shown in Fig. 2(b). Formulation of the two governing partial differential equations for membrane displacement will largely follow that in Rakhmatulin and Dem'yanov (1961).

Consider a membrane element initially of volume $hr\,\mathrm{d}r\,\mathrm{d}\phi$, where h is its initial thickness and ρ is its initial density. Conservation of mass of the element during deformation requires

$$\rho h r\,\mathrm{d}r\,\mathrm{d}\phi = \bar{\rho}\bar{h}(r+u)(1+\varepsilon_t)\,\mathrm{d}r\,\mathrm{d}\phi \tag{1}$$

where $\bar{\rho}$ and $\bar{h}$ and $(1 + \varepsilon_t)\,\mathrm{d}r$ are, respectively, its current density, thickness and length, and where ε_t is its local in-plane strain oriented radially. This strain is given by

$$\varepsilon_t = \sqrt{(1+\partial u/\partial r)^2 + (\partial v/\partial r)^2} - 1 \tag{2}$$

since the element may lie out of plane after deformation. The circumferential hoop strain ε_ϕ is

$$\varepsilon_\phi = u/r \tag{3}$$

At a given instant, forces act on the element locally in plane but radially oriented, these being $-\bar{\sigma}_t\bar{h}(r+u)\,\mathrm{d}\phi$ and $\bar{\sigma}_t\bar{h}(r+u)\,\mathrm{d}\phi + [\partial(\bar{\sigma}_t\bar{h}(r+u))/\partial r]\,\mathrm{d}r\,\mathrm{d}\phi$ where $\bar{\sigma}_t$ is the true stress. There is also a resultant force from circumferential (hoop) stresses resolved in the radial direction parallel to the ground plane and given by $-\bar{\sigma}_\phi\bar{h}(1+\varepsilon_t)\,\mathrm{d}r\,\mathrm{d}\phi$ where $\bar{\sigma}_\phi$ is the true hoop stress. Resolving these forces parallel to and perpendicular to the ground plane ($y = 0$), respectively, and using conservation of momentum leads to

$$\rho h r\,\mathrm{d}r\,\mathrm{d}\phi\,\frac{\partial^2 u}{\partial t^2} = \frac{\partial}{\partial r}\left[\bar{\sigma}_t\bar{h}(r+u)\cos\gamma\right]\mathrm{d}r\,\mathrm{d}\phi - \bar{\sigma}_\phi\bar{h}(1+\varepsilon_t)\,\mathrm{d}r\,\mathrm{d}\phi \tag{4}$$

and

$$\rho h r\,\mathrm{d}r\,\mathrm{d}\phi\,\frac{\partial^2 v}{\partial t^2} = \frac{\partial}{\partial r}\left[\bar{\sigma}_t\bar{h}(r+u)\sin\gamma\right]\mathrm{d}r\,\mathrm{d}\phi \tag{5}$$

where γ is the angle between the local tangential surface to the membrane element and the ground plane, $y = 0$. We let σ_t and σ_ϕ be the 'engineering' stresses corresponding, respectively, to $\bar{\sigma}_t$ and $\bar{\sigma}_\phi$. Comparing areas before and after deformation gives

$$\sigma_t = \bar{\sigma}_t\bar{h}(r+u)\,\mathrm{d}\phi/(h r\,\mathrm{d}\phi) \tag{6}$$

and

$$\sigma_\phi = \bar{\sigma}_\phi\bar{h}(1+\varepsilon_t)\,\mathrm{d}r/(h\,\mathrm{d}r) \tag{7}$$

Combining Eqs. (4)–(7) results in the two governing partial differential equations

$$\rho\,\partial^2 u/\partial t^2 = (1/r)\,\partial(\sigma_t r\cos\gamma)/\partial r - \sigma_\phi/r \tag{8}$$

and

$$\rho\,\partial^2 v/\partial t^2 = -(1/r)\,\partial(\sigma_t r\sin\gamma)/\partial r \tag{9}$$

where

$$\cos\gamma = (1+\partial u/\partial r)\Big/\sqrt{(1+\partial u/\partial r)^2 + (\partial v/\partial r)^2} \tag{10}$$

and

$$\sin\gamma = -(\partial v/\partial r)\Big/\sqrt{(1+\partial u/\partial r)^2+(\partial v/\partial r)^2} \tag{11}$$

The stresses and strains are related by

$$\sigma_t = [E/(1-v^2)](\varepsilon_t + v\varepsilon_\phi) \tag{12}$$

and

$$\sigma_\phi = [E/(1-v^2)](\varepsilon_\phi + v\varepsilon_t) \tag{13}$$

A crucial quantity is the speed of tensile waves in the membrane radiating outward in plane. This wave-speed, a_0, is given by $a_0^2 = E/[\rho(1-v^2)]$. To greatly simplify the upcoming analysis of cone deflection, we neglect Poisson's ratio, v, in the governing equations. In the tensile wave region outside the cone, it so happens that v appears in the governing equations, only through a_0. For materials of interest, $0 \leqslant v \leqslant 0.3$, so neglecting v in a_0 results in less than 5% error. Thus we neglect Poisson's ratio throughout and take

$$a_0 = \sqrt{E/\rho} \tag{14}$$

Initially we retain the hoop stress term to see what its influence might be, but since all hoop stresses will prove to be compressive we neglect them. Membranes and fabrics do not support significant in-plane compressive stresses as the constituent wavy yarns will buckle.

In terms of ε_t and a_0, the governing equations (8) and (9), now become

$$\frac{1}{a_0^2}\frac{\partial^2 u}{\partial t^2} = \frac{1}{r}\frac{\partial}{\partial r}(\varepsilon_t r\cos\gamma) - \left[\frac{u}{r^2}\right]^{\oplus} \tag{15}$$

and

$$\frac{1}{a_0^2}\frac{\partial^2 v}{\partial t^2} = -\frac{1}{r}\frac{\partial}{\partial r}(\varepsilon_t r\sin\gamma) \tag{16}$$

where the symbol $[\cdot]^{\oplus}$ means the quantity is kept only if positive. These equations, together with Eqs. (10) and (11) for the angle γ, constitute the system to be solved.

An important simplification is the 1D model where the material still has initial thickness h and density ρ but is formed into n equispaced, radial spokes of constant cross-sectional area $\pi r_p^2 h/n$. The total cross-sectional area of material at radial distance r is $\pi r_p^2 h$, the same as at the projectile edge r_p, and also in the 2D membrane model at radius r_p. Just two spokes yields the problem of 1D impact onto a tape. Thus taking $r = r_p$, Eqs. (15) and (16) collapse to

$$(1/a_0^2)\,\partial^2 u/\partial t^2 = \partial(\varepsilon_t\cos\gamma)/\partial r \tag{17}$$

and

$$(1/a_0^2)\,\partial^2 v/\partial t^2 = -\partial(\varepsilon_t\sin\gamma)/\partial r \tag{18}$$

3. Solution of governing partial differential equations

As key steps in solving the 2D membrane impact problem, we recognize two distinct zones: (i) a tensile "implosion" zone representing in-plane deformation whereby material behind the radially expanding, tensile wave front is drawn towards the origin at velocity $\dot{u}$, where $|\dot{u}| \ll a_0$; (ii) an expanding curved conical zone with outer edge wave front traveling at velocity c relative to the original material (Lagrangian) co-ordinates; its speed relative to ground is $\tilde{c} = c + \dot{u} < c$ since the cone grows in fabric material traveling

towards the origin. We find that $V_p < c \ll a_0$, and c turns out to be remarkably constant over the propagation regime of interest except for a very brief transition where c jumps a few percent from an initial value, c_0, calculated also from the 1D problem. The strategy is to first solve (i) and (ii) separately, and then match their solutions through mutual boundary conditions at the propagating cone edge.

3.1. Radial tension wave analysis associated with 'implosion'

In considering possible self-similar solutions to the radially expanding tensile wave, we work with the distance variable s rather than time t where

$$s = a_0 t + r_p = a_0(t + \bar{t}_p) \tag{19}$$

and $\bar{t}_p = r_p/a_0$ is the time it takes for the tension wave to travel distance r_p, the projectile cylinder radius. Note that s is the position of the tension wave front. The time shift, $\bar{t}_p$, is essential to obtaining a match to the emerging cone wave at the projectile edge when $t = 0$.

Beyond the conical wave front we have $\gamma = 0$ and $\partial u/\partial r = \varepsilon_t$ so Eq. (15) reduces to

$$\frac{\partial^2 u}{\partial s^2} = \frac{1}{r}\frac{\partial}{\partial r}\left(r\frac{\partial u}{\partial r}\right) - \left[\frac{u}{r^2}\right]^{\oplus} \tag{20}$$

while Eq. (16) for v vanishes. Eq. (20) applies to the region $r_c < r \leqslant a_0 t + r_p$, where $r_c = r_c(t)$ is the position of the cone wave front. We search for self-similar solutions of the form

$$u = u_\beta = \mu s^\beta U_\beta(\zeta) \tag{21}$$

where $\zeta = r/s$, and β and μ are constants. Substitution of Eq. (21) into Eq. (20) yields

$$\zeta^2(1-\zeta^2)U_\beta'' - \{2(1-\beta)\zeta^3 - \zeta\}U_\beta' + \beta(1-\beta)\zeta^2 U_\beta - [U_\beta]^{\oplus} = 0 \tag{22}$$

where for the time being we take the lower limit to be zero so that $0 < \zeta \leqslant 1$.

Following Grigoryan (1949), we first consider $\beta = 1$, whereby Eq. (22) reduces to

$$\zeta^2(1-\zeta^2)U_1'' + \zeta U_1' - [U_1]^{\oplus} = 0 \tag{23}$$

Neglecting $[U_1]^{\oplus}$ since U_1 is negative, and integrating the first-order equation in U_1' yields

$$U_1'(\zeta) = \sqrt{1-\zeta^2}\Big/\zeta \tag{24}$$

where the constant of integration is conveniently chosen as unity. Integrating once more and setting $u_1(1) = 0$ at the wave front (to avoid a displacement jump) results in

$$U_1(\zeta) = \left[\ln\zeta - \ln\left(1+\sqrt{1-\zeta^2}\right) + \sqrt{1-\zeta^2}\right] \tag{25}$$

Thus the form of the displacement for $\beta = 1$ is

$$u_1 = \mu s\left[\ln\zeta - \ln\left(1+\sqrt{1-\zeta^2}\right) + \sqrt{1-\zeta^2}\right] \tag{26}$$

and the associated radial strain is

$$\partial u_1/\partial r = \mu U_1'(\zeta) = \mu\sqrt{1-\zeta^2}\Big/\zeta \tag{27}$$

While $\beta = 1$ might seem to be the natural choice, the strain given by Eq. (27), approaches zero at the wave front rather than a constant as will occur in 1D. Thus the $\beta = 1$ solution disallows a strain jump (and

velocity jump) behind the tensile wave front. Thus, at the instant of projectile impact, membrane material will *not* initially be fed towards the projectile edge to allow for infinitesimal emergence of a cone-shaped deformation section, causing an instantaneous strain singularity implying perforation no matter how small V_p. Apparently this was a key concern of Rakhmatulin and Dem'yanov (1961), though they did not pursue other solutions.

Regarding another comment of Rakhmatulin and Dem'yanov (1961), it so happens that even if compressive hoop stresses are permitted, i.e., $-\sigma_\phi/r$ is kept in Eq. (8), similar behavior still results. Making the variable change $\varsigma = \zeta^2$, whereby the differential equation can be integrated in similar fashion, and then returning to the original variables, we obtain,

$$u_h = \mu s \zeta \left[\ln\left(1 + \sqrt{1-\zeta^2}\right) - \ln\zeta - \sqrt{1-\zeta^2}\Big/\zeta^2 \right] \tag{28}$$

with the strain being

$$\partial u_h/\partial r = \mu \left[\ln\left(1 + \sqrt{1-\zeta^2}\right) - \ln\zeta + \sqrt{1-\zeta^2}\Big/\zeta^2 \right] \tag{29}$$

Again the strain is zero just behind the wave front so retaining hoop stresses does not help.

Thus we must seek solutions to Eq. (22) for other values of β, which is more difficult, so we seek Frobenius series solutions in powers of ζ, as described, for example, in Boyce and DiPrima (1997). We first solve the associated Euler equation

$$\zeta^2 \widetilde{U}_\beta'' + \zeta \widetilde{U}_\beta' = 0 \tag{30}$$

and trying a solution of the form $\widetilde{U}_\beta = c\zeta^q$ yields the indicial equation $q^2 = 0$ and Euler solution

$$\widetilde{U}_\beta = c_0 + c_1 \ln\zeta \tag{31}$$

Thus a Frobenius series solution is of the form

$$U_\beta = c_0(1 + a_1\zeta + a_2\zeta^2 + \cdots) + c_1 \ln\zeta(1 + b_1\zeta + b_2\zeta^2 + \cdots) \tag{32}$$

where coefficients a_i and b_i, depend on β and must be determined recursively.

This result does not reveal the strain behavior near $\zeta = 1$, nor whether or not c_0 must be zero to satisfy $u_\beta(1) = 0$. Thus near $\zeta = 1$, we making the variable change, $\eta^2 = 1 - \zeta^2$, in Eq. (22), and appreciating that U_β will be negative so $[U_\beta]^\oplus$ vanishes, Eq. (22) takes the form

$$(1-\eta^2)\eta^2 \,\mathrm{d}^2U_\beta/\mathrm{d}\eta^2 + [2(1-\beta)(1-\eta^2) - 2]\eta \,\mathrm{d}U_\beta/\mathrm{d}\eta + [\beta(1-\beta)]\eta^2 U_\beta = 0 \tag{33}$$

The associated Euler equation is now

$$\eta^2 \,\mathrm{d}^2\widetilde{U}_\beta/\mathrm{d}\eta^2 - 2\beta\eta \,\mathrm{d}\widetilde{U}_\beta/\mathrm{d}\eta = 0 \tag{34}$$

and trying $\widetilde{U}_\beta = c\eta^q$ leads to the indicial equation $q(q - (1 + 2\beta)) = 0$. Thus the Euler solution is

$$\widetilde{U}_\beta = c_0' + c_1'\eta^{1+2\beta} \tag{35}$$

provided $\beta \neq -1/2$, which is not of interest. The Fobenius solution for U_β, upon making the replacement $\eta = \sqrt{1-\zeta^2}$, is of the form

$$U_\beta(\zeta) = c_1'\left(1 + d_1\left(\sqrt{1-\zeta^2}\right) + d_2\left(\sqrt{1-\zeta^2}\right)^2 + \cdots\right) + c_2'\left(1 + e_1\left(\sqrt{1-\zeta^2}\right) + e_2\left(\sqrt{1-\zeta^2}\right)^2 + \cdots\right)(1-\zeta^2)^{\beta+1/2} \tag{36}$$

where d_i and e_i depend on β. Also $u_\beta(1) = 0$ requires $c_1' = 0$ and taking $c_2' = -1$, Eq. (21) yields

$$u_\beta = -\mu s^\beta\left(1 + e_1\left(\sqrt{1-\zeta^2}\right) + e_2\left(\sqrt{1-\zeta^2}\right)^2 + \cdots\right)(1-\zeta^2)^{\beta+1/2} \tag{37}$$

For the strain, notice that

$$\partial u_\beta/\partial r = \mu 2(\beta+1/2)s^{\beta-1}\zeta(1-\zeta^2)^{\beta-1/2}\left\{1 + \mathrm{O}\left(\sqrt{1-\zeta^2}\right)\right\} \tag{38}$$

so $\partial u_\beta/\partial r \to 0$ as $\zeta \to 1$ for $\beta > 1/2$ but diverges for $\beta < 1/2$. For $\beta = 1/2$ we find

$$u_{1/2} = -\mu s^{1/2}\left(1 + e_1\left(\sqrt{1-\zeta^2}\right) + e_2\left(\sqrt{1-\zeta^2}\right)^2 + \cdots\right)(1-\zeta^2) \tag{39}$$

and

$$\partial u_{1/2}/\partial r = 2\mu s^{-1/2}\zeta\left\{1 + \mathrm{O}\left(\sqrt{1-\zeta^2}\right)\right\} \tag{40}$$

Thus the strain approaches a constant as $\zeta \to 1$, i.e., just behind the wave front but dies out as $s^{-1/2}$ as the wave front grows. Thus we need $\beta \geqslant 1/2$ to avoid singular strains at the wave front.

Returning to Eq. (30) for $\beta = 1/2$, it turns out that an extremely accurate approximation is

$$u_{1/2} \approx \mu s^{1/2}\ln\zeta \tag{41}$$

with the strain being

$$\sigma_r/E = \partial u_{1/2}/\partial r = \mu s^{-1/2}/\zeta \tag{42}$$

Substitution of Eq. (41) into Eq. (20) reveals that an added hoop-stress body force distribution

$$\sigma_\phi/E = \varepsilon_\phi = (1/4)\mu s^{-1/2}\zeta\ln\zeta \tag{43}$$

is sufficient to result in Eq. (41) exactly. Remarkably, this hoop contribution turns out to be negligible since the ratio σ_ϕ/σ_r is less than 0.05 for all $0 < \zeta \leqslant 1$, and is zero for $\zeta = 0$ and 1.

For fixed ζ or r, whereas the special $\beta = 1/2$ solution, $u_{1/2}$, decays relative to the $\beta = 1$ solution, u_1, as $s^{-1/2}$, it is nonetheless essential to modeling strain behavior just after impact. Rakhmatulin and Dem'yanov (1961) mentioned behavior consistent with $u_{1/2}$ but only right on the sonic wave front $r = s$ or $\zeta = 1$. The role of $u_{1/2}$ behind the wave front $\zeta < 1$ apparently was ignored. Remarkably, if one combines the $\beta = 1/2$ and $\beta = 1$ solutions in the form

$$u = \Theta_1 u_1 + \Theta_2 u_{1/2} \tag{44}$$

where $\Theta_1 \approx \Theta_2 \approx 1$, the resulting behavior differs little from the simple form

$$\tilde{u} = \mu s\ln\zeta \tag{45}$$

The associated strain and particle velocity, respectively, become

$$\partial\tilde{u}/\partial r = \mu/\zeta \tag{46}$$

and

$$\dot{\tilde{u}} \equiv \partial\tilde{u}/\partial t = a_0\partial\tilde{u}/\partial s = a_0\mu(\ln\zeta - 1) \tag{47}$$

This solution has the required jumps in strain and particle velocity at the wave front. Furthermore it can be shown that if Eq. (20) is differentiated with respect to r to yield a partial differential equation in radial strain, Eq. (45) is a solution. It is not, however, directly a solution to Eq. (20) without adding a modest body force term that fortunately, does not affect the strains.

In the case of the 1D model with the radially expanding tension wave, Eq. (17) reduces to

$$\partial^2 u/\partial s^2 = \partial^2 u/\partial r^2 \tag{48}$$

compared to Eq. (20) in 2D, and Eq. (18) for v vanishes. Substituting Eq. (21) yields

$$(1-\zeta^2)U_\beta'' + 2(\beta-1)\zeta U_\beta' - \beta(\beta-1)U_\beta = 0 \tag{49}$$

for general β where $0 < \zeta \leqslant 1$. For $\beta = 1$, Eq. (49) simplifies to

$$(1-\zeta^2)U_1'' = 0 \tag{50}$$

and since $1-\zeta^2 \neq 0$ except at $\zeta = 1$ we must have $U_1'' = 0$, which integrates to give

$$U_1 = A_1 + A_2\zeta \tag{51}$$

where A_1 and A_2 are constants. To avoid a displacement jump at the tensile wave front that would imply tape failure, we need $U_1(1) = 0$ requiring $A_2 = -A_1 = 1$ so that

$$U_1 = -(1-\zeta) \tag{52}$$

The corresponding strain is

$$\partial u_1/\partial r = \partial(\mu s U_1)/\partial r = \mu U_1' = \mu \tag{53}$$

which is a constant, and designating the strain μ as ε_t, Eqs. (21) and (52) yield

$$u_1 = \mu s U_1(\zeta) = -\varepsilon_t s(1-\zeta) \tag{54}$$

The velocity of material behind the wave front is

$$\dot{u}_1 \equiv \partial u_1/\partial t = a_0\varepsilon_t\{U_1(\zeta) - \zeta U_1'(\zeta)\} = -a_0\varepsilon_t \tag{55}$$

In 1D, other values of β turn out to be physically irrelevant to constant velocity impact. The case $\beta = 0$ yields unbounded displacements at the wave front. For other values $0 < \beta < 1$, a Frobenius series solution in Eq. (49) together with the change of variable $\eta = \sqrt{1-\zeta^2}$ yields a singular strain at the wave front implying instant failure. For $\beta > 1$ the displacement and the strain decay to zero as $\zeta \to 1$, as does the material velocity, $\dot{u}_\beta \equiv \partial u_\beta/\partial t$, towards the impact point. These features are incompatible with the required velocity flow of material into the edge of the impact cone or triangle allowing it to develop behind the tension wave with finite strain.

In 1D, the case $\beta = 1$ is special in that there is a negative velocity jump as well as a strain jump at the tensile wave front from zero ahead of it to ε_t behind it. A self-similar solution with displacements proportional to time might seem obvious as the only solution relevant to constant projectile velocity. For the 2D membrane, however, the case $\beta = 1/2$ is the relevant one at early times, and the case $\beta = 1$, becomes important somewhat later. The approximate solution, Eq. (45), captures both features: A small distance back from the tensile wave front, but in front of the cone wave front, Eq. (45) quickly takes on the behavior of Eq. (26). Right near and at the tensile wave front, however, it has the behavior of Eq. (41) just long enough to allow the cone wave to emerge with locally finite strain. We will find that as the impact cone

emerges from the projectile edge, within one projectile radius r_p of cone growth a sharp transition zone exists where the cone edge velocity rapidly rises from an initial 1D value, but then stabilizes to almost constant behavior. The membrane strain is *not* infinite upon impact but actually begins with 1D like behavior before increasing rapidly, with a strain concentration emerging and continuing to grow adjacent to the projectile. Not accounting for such features seems to be at the heart of the pessimism expressed by Rakhmatulin and Dem'yanov (1961).

For the 2D membrane, we use the approximate solution, Eq. (45), as the primary solution for the in-plane, implosion wave and match boundary conditions with the growing cone wave just after impact. In our impact problem, tensile tractions and displacements must be properly matched at the edge of the growing deformation cone, especially just after impact. The later success of the approximation, Eq. (45), suggests that the actual solution u under constant projectile velocity V_p may well be a weighted integral over $1/2 \leqslant \beta \leqslant 1$ of solutions u_β with the endpoints, 1/2 and 1, strongly dominating. Pursuit of this feature, however, is not necessary for us to achieve accurate results, because of the overwhelming dominance of the rapid transition.

3.2. Self-similarity transformation and cone wave analysis

Following impact on the membrane, a curved-sided, truncated cone develops in the wake of the tensile implosion wave, the latter supplying the necessary displacements at the cone outer edge to allow large cone angles. The key is to seek a self-similar solution based on the cone wave front velocity, c, rather than the tension wave velocity, a_0, assuming c is constant. Under constant projectile velocity, V_p, we will find that c is not quite constant, but is very close to constant after an extremely short transition region of growth where c rapidly jumps up from the starting 1D value, denoted c_0. A slightly varying c in the self-similar solution still yields an extremely accurate representation of impact behavior since $V_p/a_0 < c/a_0 \ll 1$, thus permitting the strains and other quantities to rapidly self-adjust. We are ultimately interested in an analysis of deceleration of the projectile due to reactive forces of the membrane, so following the transition after impact, the cone wave speed c will decrease fairly rapidly tending to offset the increase mentioned above. We proceed here under the assumption that c is constant.

We let $\alpha = c/a_0$ be the ratio of cone wave speed to tension wave speed and develop a self-similar solution in terms of the cone wave, travel distance variable

$$z = ct + r_p = \alpha a_0(t + t_p) \tag{56}$$

where $t_p = r_p/c$, is the time it takes for the cone wave to travel the distance r_p. Note that $t_p = \bar{t}_p/\alpha$ so the time shifts are different for the tension and cone waves. However, this relationship will allow us to properly match the mutual boundary conditions of the two waves as the leading edges of both coincide at the edge of the projectile at r_p at the time of impact, $t = 0$. Note that z can also be interpreted as the position of the cone wave front, r_c, at time t.

In terms of z rather than t, the partial differential equations (15) and (16) become

$$\alpha^2 \frac{\partial^2 u}{\partial z^2} = \frac{1}{r}\frac{\partial}{\partial r}(\varepsilon_t r \cos\gamma) \tag{57}$$

and

$$\alpha^2 \frac{\partial^2 v}{\partial t^2} = -\frac{1}{r}\frac{\partial}{\partial r}(\varepsilon_t r \sin\gamma) \tag{58}$$

with Eqs. (10) and (11) for $\cos\gamma$ and $\sin\gamma$ unchanged. Henceforth we neglect the square bracketed term in Eq. (15) since the displacement u is negative. We let

$$X(\xi) = (u + r)/z = (u/r)\xi + \xi \tag{59}$$

and

$$Y(\xi) = v/z = (v/r)\xi \tag{60}$$

where $\xi = r/z$. We interpret X and Y as the new positions of a fabric particle originally at r in undeformed fabric. Then in these normalized coordinates (in terms of material rather than ground coordinates) the cone wave front or base radius r_c coincides with $\xi = 1$ and the radius of the projectile inside which fabric contact occurs is $\xi_p = r_p/(\alpha s)$. Thus we obtain solutions for the region $\xi_p \leqslant \xi \leqslant 1$. Knowing $X(\xi)$ and $Y(\xi)$, we can obtain the displacements u and v.

First we substitute Eqs. (59) and (60) into Eqs. (2), (10), (11), (57) and (58), and using the notation $(\cdot)' \equiv \mathrm{d}(\cdot)/\mathrm{d}\xi$ we obtain

$$\alpha^2\xi^3 X''(\xi) = (\xi\varepsilon_t \cos\gamma)' \tag{61}$$

and

$$\alpha^2\xi^3 Y''(\xi) = -(\xi\varepsilon_t \sin\gamma)' \tag{62}$$

where

$$\sin\gamma = -Y'(\xi)\Big/\sqrt{X'(\xi)^2 + Y'(\xi)^2} \tag{63}$$

and

$$\cos\gamma = X'(\xi)\Big/\sqrt{X'(\xi)^2 + Y'(\xi)^2} \tag{64}$$

and ε_t is the local membrane strain (perpendicular to the circumferential direction) given by

$$\varepsilon_t = \sqrt{X'(\xi)^2 + Y'(\xi)^2} - 1 \tag{65}$$

It is convenient to let

$$R = \sqrt{X'(\xi)^2 + Y'(\xi)^2} = \varepsilon_t + 1 \tag{66}$$

Multiplying the equations in X'' and Y'' by X' and Y', respectively, and using the fact that $(X'^2)' = 2X'X''$(and likewise for Y) and then adding the two resulting equations leads to

$$\alpha^2\xi^3 R' = R - 1 + \xi R' \tag{67}$$

Because $\varepsilon_t = R - 1$ and $R' = (R - 1)'$ this can be written as

$$\xi(1 - \alpha^2\xi^2)\varepsilon_t' + \varepsilon_t = 0 \tag{68}$$

This same exercise also yields key differential equations for X and Y, which are

$$\xi(1 - \alpha^2\xi^2)X'' + X' = (\xi X'/R)' \tag{69}$$

and

$$\xi(1 - \alpha^2\xi^2)Y'' + Y' = (\xi Y'/R)' \tag{70}$$

These can be manipulated to yield

$$\alpha^2\xi^3 X'' = (\xi(R - 1)X'/R)' \tag{71}$$

and

$$\alpha^2\xi^3 Y'' = (\xi(R-1)Y'/R)' \tag{72}$$

In 1D the same procedure yields simpler differential equations, namely

$$\xi(1-\alpha^2\xi^2)\varepsilon_t' = 0 \tag{73}$$

together with

$$\alpha^2\xi^2 X'' = ((R-1)X'/R)' \tag{74}$$

and

$$\alpha^2\xi^2 Y'' = ((R-1)Y'/R)' \tag{75}$$

which are much easier to solve.

3.3. Solution for radial and transverse displacement functions for small strains

In 2D we first solve Eq. (68) for ε_t to yield R, and then to solve Eqs. (71) and (72) for X and Y, respectively. Solving for ε_t is straightforward since Eq. (68) can be directly integrated to yield

$$\int \frac{\mathrm{d}\varepsilon_t}{\varepsilon_t} = -\int \frac{\mathrm{d}\xi}{\xi(1-\alpha^2\xi^2)} = \frac{1}{2}\int \frac{\mathrm{d}(1-w^2)}{1-w^2} - \int \frac{\mathrm{d}w}{w} \tag{76}$$

where $w = \alpha\xi$. Thus

$$\ln\varepsilon_t = (1/2)\ln(1-w^2) - \ln w + \ln C \tag{77}$$

which is equivalent to

$$\varepsilon_t = C\sqrt{1-\alpha^2\xi^2}\Big/(\alpha\xi) \tag{78}$$

where C is a constant of integration. At the outer cone edge, $\xi = 1$, we define $\varepsilon_c \equiv \varepsilon_t(1)$, which is matched with a like strain quantity from the implosion plane-wave solution. We then have

$$\varepsilon_t = \frac{\varepsilon_c}{\xi}\frac{\sqrt{1-\alpha^2\xi^2}}{\sqrt{1-\alpha^2}} = \frac{\varepsilon_c}{\xi}\left\{1 + \frac{\alpha^2}{2}(1-\xi^2) + \frac{3\alpha^4}{8}(1-\xi^4) + \cdots\right\}, \quad \xi_p \leqslant \xi \leqslant 1 \tag{79}$$

At the projectile edge we define $\varepsilon_p \equiv \varepsilon_t(\xi_p)$ and this is the maximum strain in the membrane. We discover that we must have $\alpha^2 = \varepsilon_p < \varepsilon_{max}\xi_p$ to avoid membrane failure and perforation, where typically $\varepsilon_{max} < 0.05$ for materials of interest. Thus Eq. (79) is approximately

$$\varepsilon_t(\xi) \approx \varepsilon_c/\xi, \quad \xi_p \leqslant \xi \leqslant 1 \tag{80}$$

with less than 1% error. In what follows we assume this condition is satisfied.

Next we solve Eq. (72) for Y and first note from the above that

$$R = 1 + \varepsilon_t \approx 1 + \varepsilon_c/\xi \tag{81}$$

which upon substitution into Eq. (72) yields

$$\alpha^2\xi^3 Y'' \approx \{\varepsilon_c\xi Y'/(\xi+\varepsilon_c)\}' \tag{82}$$

Carrying out the differentiation on the right-hand side and rearranging the result yields

$$\xi(\xi+\varepsilon_c)\{\alpha^2\xi^2(\xi+\varepsilon_c) - \varepsilon_c\}Y'' - \varepsilon_c^2 Y' \approx 0 \tag{83}$$

In preparation for integration, this may be rewritten as

$$dY'/Y' \approx (\varepsilon_c/\alpha)^2 d\xi/\{\xi(\xi+\varepsilon_c)(\xi^3+\varepsilon_c\xi^2-\varepsilon_c/\alpha^2)\} \tag{84}$$

where it then becomes necessary to factor the cubic using well-known formulas. Recognizing the maximum strain constraint above, we obtain the accurate approximation

$$\xi^3+\varepsilon_c\xi^2-\varepsilon_c/\alpha^2 \approx (\xi+\varepsilon_c/3)^3-\varphi^3 \tag{85}$$

where

$$\varphi = (\varepsilon_c/\alpha^2)^{1/3} \tag{86}$$

In the above differential, making the respective substitutions $\xi+\varepsilon_c \approx \xi+\varepsilon_c/3$, and $\xi \approx \xi+\varepsilon_c/3$ will not affect the results of integration since to avoid perforation, $\varepsilon_c/\varepsilon_{max} \leqslant \xi_p \leqslant \xi \leqslant 1$ and typically $\varepsilon_{max} < 0.05$. Thus we may reduce our differential approximation, Eq. (84), to

$$d(-Y')/(-Y') \approx -\varepsilon_c\varphi^3 d\xi/\{(\xi+\varepsilon_c/3)^2[\varphi^3-(\xi+\varepsilon_c/3)^3]\} \tag{87}$$

in anticipation that $\xi+\varepsilon_c/3 \leqslant \varphi$ for $\xi_p \leqslant \xi \leqslant 1$, and that Y' will be negative since the cones slope is negative. Eq. (87) decomposes as

$$\int d(-Y')/(-Y') \approx -\varepsilon_c \int d\xi/(\xi+\varepsilon_c/3)^2 - \varepsilon_c \int (\xi+\varepsilon_c/3)\, d\xi/\{\varphi^3-(\xi+\varepsilon_c/3)^3\} \tag{88}$$

and carrying out the integration results in

$$\ln(-Y') \approx \frac{\varepsilon_c}{\xi+\varepsilon_c/3} - \frac{\varepsilon_c}{6\varphi}\ln\left\{\frac{\varphi^3-(\xi+\varepsilon_c/3)^3}{[\varphi-(\xi+\varepsilon_c/3)]^3}\right\} + \frac{\varepsilon_c}{\sqrt{3}\varphi}\tan^{-1}\left(\frac{2(\xi+\varepsilon_c/3)+\varphi}{\sqrt{3}\varphi}\right) + \ln\kappa_1 \tag{89}$$

where κ_1 is a constant of integration to be determined later. Exponentiation gives

$$Y' \approx -\kappa_1 \exp\left(\frac{\varepsilon_c}{\xi+\varepsilon_c/3}\right)\left\{\frac{[\varphi-(\xi+\varepsilon_c/3)]^3}{\varphi^3-(\xi+\varepsilon_c/3)^3}\right\}^{\varepsilon_c/6\varphi} \exp\left[\frac{1}{\sqrt{3}}\frac{\varepsilon_c}{\varphi}\tan^{-1}\left(\frac{2(\xi+\varepsilon_c/3)+\varphi}{\sqrt{3}\varphi}\right)\right] \tag{90}$$

To interpret this result, we first assert (with later comment) that $\varphi \approx 1+\varepsilon_c/3$, since this will ensure no singularity in Y' except at the end point $\xi = 1$. From this we see that

$$\varepsilon_c/\alpha^2 = (1+\varepsilon_c/3)^3 \approx 1+\varepsilon_c \tag{91}$$

yielding

$$\alpha = c/a_0 \approx \sqrt{\varepsilon_c/(1+\varepsilon_c)} \tag{92}$$

for the transverse wave speed c of the cone edge. In subsequent analysis $\alpha \approx \sqrt{\varepsilon_c}$ will suffice.

Whereas the result above for Y' appears complicated, it has a very simple approximation. To avoid perforation we require $\varepsilon_c \leqslant \varepsilon_{max}\xi_p \leqslant 0.05\xi_p$, and for the cone edge, $r_c = r_p/\xi_p$, to grow even a modest distance we must have $\varepsilon_c < 0.01$. In that case the exponential factor in Y' with the inverse tangent deviates from unity by only 1% over the range $\xi_p \leqslant \xi \leqslant 1$ irrespective of ξ_p. Also, since $\varepsilon_c/(6\varphi) \ll 0.01$, the middle factor is unity to within 1% over $\xi_p \leqslant \xi \leqslant 0.99$. It then rapidly drop to zero as $\xi \to 1$, which implies that the membrane slope, Y', approaches zero as $r \to r_c$, a feature seen experimentally but of no practical consequence in the analysis. Finally, there is virtually no loss in accuracy in replacing $\xi+\varepsilon_c/3$ with ξ in the first exponential, whose form also implies mild cone curvature. Thus, an extremely accurate approximation is

$$Y' \approx -\kappa_1 e^{\varepsilon_c/\xi} \tag{93}$$

The same analysis works on Eq. (61) except that X' is positive. Consequently we get

$$X' \approx \kappa_2 \, \mathrm{e}^{\varepsilon_c/\xi} \tag{94}$$

Next we develop a relationship between κ_1 and κ_2, which are not independent. Since $R = 1 + \varepsilon_t \approx 1 + \varepsilon_c/\xi$, we develop Taylor series expansions for X' and Y' to find that

$$1 + \varepsilon_c/\xi \approx \sqrt{\kappa_1^2 + \kappa_2^2}(1 + (\varepsilon_c/\xi) + (1/2)(\varepsilon_c/\xi)^2 + \cdots) \tag{95}$$

so to very high accuracy

$$\kappa_1^2 + \kappa_2^2 \approx 1 \tag{96}$$

We can integrate Eqs. (93) and (94) to get Y and X, respectively, and from geometric considerations the out of plane displacement at the projectile edge must be that of the projectile nose, and the in plane displacement must be zero (i.e., $X(\xi_p) = \xi_p$). Thus we can write

$$X \approx \kappa_2 \int_{\xi_p}^{\xi} \mathrm{e}^{\varepsilon_c/w} \, \mathrm{d}w + \xi_p \tag{97}$$

and

$$Y \approx \kappa_1 \int_{\xi}^{1} \mathrm{e}^{\varepsilon_c/w} \, \mathrm{d}w \tag{98}$$

The variable change $x = 1/w$ gives an integral that can be evaluated to produce the series

$$\int (\mathrm{e}^{\varepsilon_c x}/x^2) \, \mathrm{d}x = -\mathrm{e}^{\varepsilon_c x}/x + \varepsilon_c \ln x + \varepsilon_c^2 x + \cdots \tag{99}$$

Thus X and Y become

$$X(\xi) \approx \kappa_2 \{\xi \, \mathrm{e}^{\varepsilon_c/\xi} - \xi_p \, \mathrm{e}^{\varepsilon_c/\xi_p} + \varepsilon_c(\ln \xi - \ln \xi_p) + \varepsilon_c^2(1/\xi_p - 1/\xi) + \cdots\} + \xi_p \tag{100}$$

and

$$Y(\xi) \approx \kappa_1 \{\mathrm{e}^{\varepsilon_c} - \xi \, \mathrm{e}^{\varepsilon_c/\xi} - \varepsilon_c \ln \xi + \varepsilon_c^2(1/\xi - 1) + \cdots\} \tag{101}$$

respectively, for $\xi_p \leqslant \xi \leqslant 1$. We can also expand the exponential in this last result to obtain

$$Y(\xi) \approx \kappa_1 \{(1 - \xi) - \varepsilon_c \ln \xi + (\varepsilon_c^2/2)(1/\xi - 1)\} \tag{102}$$

to very high accuracy. This result also suggests small cone curvature.

The displacement components u and v are $u = zX(r/z) - r$ and $v = zY(r/z)$, where $z = ct + r_p = \alpha a_0(t + t_p)$. We must still evaluate the constants κ_1 and κ_2 from the initial and boundary conditions right after projectile impact, as is done next.

In 1D a similar analysis leads to that fact that ε_t is a constant and Eq. (75) yields

$$(\alpha^2 \xi^2 - \varepsilon_t/(1 + \varepsilon_t))Y'' = 0 \tag{103}$$

The term in brackets cannot be zero so solving $Y'' = 0$ gives

$$Y = C_1 + C_2 \xi \tag{104}$$

where C_1 and C_2 are constants to be evaluated. A similar analysis of Eq. (74) gives

$$X = D_1 + D_2 \xi \tag{105}$$

where D_1 and D_2 are also constants to be evaluated. The quantity in brackets in Eq. (103) is claimed to be zero right at $\xi = 1$ as this leads to a completely consistent solution that will satisfy the differential equation and boundary conditions. This claim can be verified more elaborately using the method of characteristics

on the system of partial differential equations as in Rakhmatulin and Dem'yanov (1961), or Craggs (1954). Thus the wave speed ratio α satisfies

$$\alpha = c/a_0 = \sqrt{\varepsilon_c/(1+\varepsilon_c)} \tag{106}$$

which is the same as Eq. (92) for the 2D membrane, except in the 1D case the strain is constant, i.e., $\varepsilon_t = \varepsilon_c = \varepsilon_p$, so α and c are constant in time (for constant velocity impact). In 2D α shows a rapid rise before the cone has grown in diameter by one projectile width.

3.4. Determining κ_1 and κ_2 from initial and boundary conditions

In 2D we are particularly interested in $Y(\xi_p)$ and $X(1)-1$, which represent the projectile and cone inner edge displacement and the displacement towards the origin of membrane material near the cone outer edge (i.e., amount of extra membrane material fed into the cone). The latter allows the frequently observed, large cone surface angles without exceeding the strain limit of the membrane. Expanding in Eq. (100) yields the extremely accurate approximation

$$X(1)-1 \approx \kappa_2\{(1-\xi_p) - \varepsilon_c \ln \xi_p + (\varepsilon_c^2/2)(1/\xi_p - 1) + \cdots\} - (1-\xi_p) \tag{107}$$

and Eq. (102) yields

$$Y(\xi_p) \approx \kappa_1\{(1-\xi_p) - \varepsilon_c \ln \xi_p + (\varepsilon_c^2/2)(1/\xi_p - 1) + \cdots\} \tag{108}$$

Following impact we must match the displacement of the top of the truncated cone to the projectile velocity multiplied by the *elapsed* time from impact. Since we are working with a self-similar solution for the growing cone, in terms of time $t + t_p$, we in effect account for its virtual growth from the origin ($r = 0$) at time $t = -t_p$ until the base reaches radius r_p at time $t = 0$. Up to that time there is no physical cone so the impact time corresponds to the cone wave front coinciding with $r = r_p$ when $\xi_p = 1$. Matching displacements gives $V_p t = (r_p/\xi_p)Y(\xi_p)$ or

$$V_p t = (r_p/\xi_p)\kappa_1\{1 - \xi_p - \varepsilon_c \ln \xi_p + (\varepsilon_c^2/2)(1-\xi_p)/\xi_p + \cdots\} \tag{109}$$

However, $\xi_p = r_p/r_c$ and $r_c = z = ct + r_p$ so we can rewrite this as

$$(V_p/c)(r_c - r_p) = \kappa_1 r_c\{(r_c - r_p)/r_c + \varepsilon_c \ln(r_c/r_p) + (\varepsilon_c^2/2)(r_c - r_p)/r_c + \cdots\} \tag{110}$$

Due to our constraints on maximum strain, the last term on the right is most certainly negligible; the second term, though also very small, is retained since it will have an appreciable effect on the results due to certain cancellation effects in other terms. Thus we rewrite the above result as

$$(V_p/c)(r_c - r_p) \approx \kappa_1(r_c - r_p)\{1 + \varepsilon_c[r_c/(r_c - r_p)]\ln(r_c/r_p)\} \tag{111}$$

Canceling $r_c - r_p$ from both sides and noting $1/(1+w) = 1 - w + w^2 - \cdots$ we approximate κ_1 as

$$\kappa_1 \approx \frac{V_p}{c}\left\{1 - \varepsilon_c\left(\frac{r_c}{r_c - r_p}\right)\ln\left(\frac{r_c}{r_p}\right)\right\} = \frac{V_p}{c}\left\{1 - \varepsilon_c\left(\frac{r_c}{r_p}\right)\frac{\ln(1 + (r_c - r_p)/r_p)}{(r_c - r_p)/r_p}\right\} \tag{112}$$

where there is no need for additional terms to retain accuracy. Indeed since

$$\varepsilon_c(r_c/r_p) = (r_c/\xi_p) < 0.05 \tag{113}$$

and for $r_c > r_p$

$$\ln(1 + (r_c - r_p)/r_p) < (r_c - r_p)/r_p \tag{114}$$

the second term in the curly brackets can never be more than 5% of the total as perforation would occur first. For instance if perforation occurs when $r_c = 1.5r_p$, then $\ln(1.5)/0.5 = 0.810$ so the second term is at

most 4% of the total. On the other hand if $r_c = 10r_p$ when perforation occurs, then $\ln(10)/9 = 0.256$ so the second term is only about 1% of the total. One sees that $\kappa_1 \approx V_p/c$.

3.5. Displacements and inflow of membrane at the cone edge

Next we calculate the displacement (inflow of membrane material) at the cone edge, which we call u_c and note that $u_c = r_c\{X(1) - 1\}$ or

$$u_c \approx -r_c(1-\kappa_2)(1-\xi_p) - r_c\kappa_2\{\varepsilon_c \ln \xi_p - (\varepsilon_c^2/2)(1/\xi_p - 1)\} \tag{115}$$

As before we can neglect the last term and noting $\xi_p = r_p/r_c$ rewrite the above as

$$u_c \approx -(r_c - r_p)(1-\kappa_2) - r_c\kappa_2\varepsilon_c \ln(r_p/r_c) \tag{116}$$

Earlier we established that $\kappa_1^2 + \kappa_2^2 = 1$ so

$$\kappa_2 = \sqrt{1-\kappa_1^2} \approx 1 - \kappa_1^2/2 + \kappa_1^4/8 - \cdots \tag{117}$$

Since $\kappa_1 \approx V_p/c$, the importance of the third term depends on its relative magnitude. Typically $\kappa_1 \leqslant 0.5$, so the third term is likely to be no more than 5% of the second and completely negligible relative to the first. Thus replacement of κ_2 in terms of κ_1 in the above expression for u_c requires keeping terms according to their contribution yielding

$$u_c \approx -(r_c - r_p)(\kappa_1^2/2 + \kappa_1^4/8) - r_c(1 - \kappa_1^2/2)\varepsilon_c \ln(r_p/r_c) \tag{118}$$

We can no longer ignore the term with the logarithmic factor, and the like term in κ_1 also plays a role. Substituting for κ_1 using Eq. (112) expanding and keeping the most dominant terms, and recalling that the cone edge strain and wave speed ratio are related by $\varepsilon_c \approx \alpha^2$ gives

$$u_c \approx -(r_c - r_p)\left\{\frac{1}{2}\left(\frac{V_p}{c}\right)^2 + \frac{1}{8}\left(\frac{V_p}{c}\right)^4 + \left(1 + \frac{1}{2}\left(\frac{V_p}{c}\right)^2\right)\alpha^2 \frac{\ln(1-(r_c-r_p)/r_c)}{(r_c-r_p)/r_c}\right\} \tag{119}$$

and for moderate $r_c - r_p$ we can expand the logarithm in Eq. (119) to achieve

$$\begin{aligned} u_c \approx -(r_c - r_p)\{&(1/2)(V_p/c)^2 + (1/8)(V_p/c)^4 - \alpha^2(1 + (1/2)(V_p/c)^2)(1 + (1/2)[(r_c - r_p)/r_c] \\ &+ (1/3)[(r_c - r_p)/r_c]^2 + \cdots)\} \end{aligned} \tag{120}$$

In 1D a similar procedure is followed, starting with Eqs. (104)–(106), yielding

$$u_c = -(r_c - r_p)\left(1 - \sqrt{(1+\alpha^2)^2 - (V_p/c)^2}\right) \tag{121}$$

but here α is constant in time.

3.6. Matching cone and implosion wave displacements and determining the wave speed ratio

We must now match the displacement at the cone boundary with that from the appropriate region of the in-plane implosion solution. At $t = 0$, the wave fronts of the implosion and the cone waves must coincide at the projectile radius, r_p. This requirement was anticipated using the respective time shifts $\bar{t}_p = r_p/a_0$ and $t_p = r_p/c$ whereby the times for the tension and cone waves are $t + \bar{t}_p$ and $t + t_p$, respectively. From the implosion analysis, Eq. (45) is written as

$$u_c \approx \tilde{u}(\zeta_c) = s\mu \ln \zeta_c \tag{122}$$

where $\zeta_c = r_c/s$ and $s = a_0(t + \bar{t}_p)$. Since $\varepsilon_c = \mu/\zeta_c$ and $\alpha^2 = \varepsilon_c$ we can rewrite this as

$$u_c \approx \alpha^2 r_c \ln\{r_c/(a_0(t + \bar{t}_p))\} \tag{123}$$

Since $a_0 = c/\alpha$, $t = r_c/c - t_p$ and $t_p = r_p/c$, this can be reduced to

$$u_c \approx -\alpha^2 r_c \ln\{1 + (1-\alpha)(r_c - r_p)/(\alpha r_c)\} = \alpha^2 r_c\{\ln\alpha - \ln(1 - (1-\alpha)r_p/r_c)\} \tag{124}$$

Note that when $r_c - r_p \ll 2\alpha r_p$, that is, the cone has grown only a very small fraction of the projectile diameter, we expand the logarithm in the first expression in Eq. (124) to yield

$$u_c \approx -\alpha(1-\alpha)(r_c - r_p)\{1 - (1-\alpha)(r_c - r_p)/(2\alpha r_c) - \cdots\} \tag{125}$$

For larger $r_c > r_p$ the last expression in Eq. (124) expands to

$$u_c \approx \alpha^2 r_c\{\ln\alpha + (1-\alpha)r_p/r_c + (1/2)((1-\alpha)r_p/r_c)^2 + (1/3)((1-\alpha)r_p/r_c)^3 + \cdots\} \tag{126}$$

which has about 10% error for $r_c = 1.5r_p$ that drops rapidly as r_c increases further.

To see how the deformation cone evolves, we first consider early cone growth over $0 < r_c - r_p < \alpha r_p/2$, and let $\alpha_0 = c_0/a_0$ be the initial velocity ratio, where c_0 is the initial cone wave speed just after impact. Comparing the two expressions for u_c, Eqs. (119) and (125), canceling $r_c - r_p$ from both sides and taking the limit as $r_c - r_p \to 0^+$ (i.e., $t \to 0^+$) we obtain

$$\alpha_0(1-\alpha_0) \approx (1/2)(V_p/(\alpha_0 a_0))^2 + (1/8)(V_p/(\alpha_0 a_0))^4 - \alpha_0^2 - (\alpha_0^2/2)(V_p/(\alpha_0 a_0))^2 \tag{127}$$

Neglecting the smallest term and canceling α_0^2 from both sides yields

$$(1/4)(V_p/a_0)^4 + \alpha_0^2(V_p/a_0)^2 - 2\alpha_0^5 \approx 0 \tag{128}$$

This may be factored and the relevant root yields

$$V_p/a_0 \approx \sqrt{2}\alpha_0^{3/2}(1 - \alpha_0/4) \approx \sqrt{2}\varepsilon_0^{3/4}(1 - \sqrt{\varepsilon_0}/4) \tag{129}$$

where ε_0 is the initial membrane strain at the location of projectile edge on contact, i.e. when $r_c = r_p$ and $t = 0^+$, so that, $\varepsilon_0 \approx \alpha_0^2$, as mentioned in connection with Eq. (92). Inversion in Eq. (129) yields an approximation for α_0 in terms of V_p, which is

$$\alpha_0 \approx (V_p/(\sqrt{2}a_0))^{2/3}\{1 + (1/6)(V_p/(\sqrt{2}a_0))^{2/3}\} \approx (V_p/(\sqrt{2}a_0))^{2/3} \tag{130}$$

The initial cone edge wave speed relative to material coordinates is $c_0 = \alpha_0 a_0$. The second factor in curly brackets is typically negligible (<3%), so in later calculations we neglect it.

In the 1D case, a similar analysis to that above leads to a similar result to Eq. (129), i.e.,

$$V_p/a_0 = \sqrt{2\varepsilon_0\sqrt{\varepsilon_0(1+\varepsilon_0)} - \varepsilon_0^2} \approx \sqrt{2}\varepsilon_0^{3/4}(1 - \sqrt{\varepsilon_0}/4) \tag{131}$$

except that the strain remains constant as $\varepsilon_t = \varepsilon_c = \varepsilon_p = \varepsilon_0$. The wave speed ratio is

$$\alpha_0 = c_0/a_0 = \sqrt{\varepsilon_0/(1+\varepsilon_0)} \tag{132}$$

that is, the cone wave speed c remains constant at c_0. Eq. (131) yields the simple approximation

$$\varepsilon_0 \approx (V_p/(\sqrt{2}a_0))^{4/3} \tag{133}$$

the "classified" result mentioned by Ringleb (1957), but originally due to Rakhmatulin (1945).

In a 2D membrane, since the speed of the tension wave front is $1/\alpha$ times the wave speed of the cone edge (i.e., larger by an order of magnitude), this 1D-like result corresponds approximately to the tension wave front being at $s = 3r_p/2$, which means that the tension wave has traveled less than the projectile radius, r_p. Beyond this point, if the strain ε_c were then to remain fixed at the 1D value, ε_0, the flow of membrane

material into the cone edge would have to slow down, since the strain at the tension wave front decreases with expanding circumference. This implies that ε_c must initially increase as the cone radius grows in order to maintain the inward flow of material, and the wave speed ratio α must also increase. We find that most of this increase occurs very quickly after impact, when the cone has grown only a small fraction of r_p. Thus the constant cone wave speed assumption needed for self-similarity is only violated significantly in this small transition region where details of impact are obscured in the first place.

To determine α as the cone grows, we keep the most dominant terms in the cone edge displacement relationships, Eqs. (119) and (125), and dividing both by r_p, we obtain

$$-\alpha^2\left\{\ln\left(\frac{1}{\alpha}\right)+\ln\left(1-\frac{(1-\alpha)r_p}{r_c}\right)\right\}\frac{r_c}{r_p}\approx-\frac{1}{2}\left(\frac{V_p}{\alpha a_0}\right)^2\frac{r_c-r_p}{r_p}+\alpha^2\frac{r_c}{r_p}\ln\left(\frac{r_c}{r_p}\right) \tag{134}$$

This can be rearranged to give

$$V_p/a_0\approx\alpha^2\sqrt{(2/(1-r_p/r_c))\ln\{1+(1/\alpha)(r_c/r_p-1)\}} \tag{135}$$

or

$$V_p/(\sqrt{2}a_0)\approx\alpha^{3/2}\sqrt{(r_c/r_p)\ln\{1+(1/\alpha)(r_c/r_p-1)\}/\{(1/\alpha)(r_c/r_p-1)\}} \tag{136}$$

If desired, we can solve for α iteratively starting with the initial 1D value $\alpha_0\approx\{V_p/(\sqrt{2}a_0)\}^{2/3}$. A first approximation for α is thus

$$\alpha_1=\left(\frac{V_p}{a_0\sqrt{2}}\right)^{2/3}\left(\frac{r_p}{r_c}\right)^{1/3}\left\{\frac{1}{\alpha_0}\left(\frac{r_c}{r_p}-1\right)\right\}^{1/3}\Bigg/\left\{\ln\left[1+\frac{1}{\alpha_0}\left(\frac{r_c}{r_p}-1\right)\right]\right\}^{1/3} \tag{137}$$

which gives results a few percent too high, but the second approximation is quite accurate, i.e.,

$$\alpha\approx\alpha_2=\left(\frac{V_p}{a_0\sqrt{2}}\right)^{2/3}\left(\frac{r_p}{r_c}\right)^{1/3}\left\{\frac{1}{\alpha_1}\left(\frac{r_c}{r_p}-1\right)\right\}^{1/3}\Bigg/\left\{\ln\left[1+\frac{1}{\alpha_1}\left(\frac{r_c}{r_p}-1\right)\right]\right\}^{1/3} \tag{138}$$

Fig. 3 plots the normalized wave speed $c/c_0=\alpha/\alpha_0$, versus the normalized cone radius $\psi=r_c/r_p$ for various values of the initial 1D strain $\varepsilon_0\approx\{V_p/(\sqrt{2}a_0)\}^{4/3}$, as calculated by iteration in Eq. (136). In all

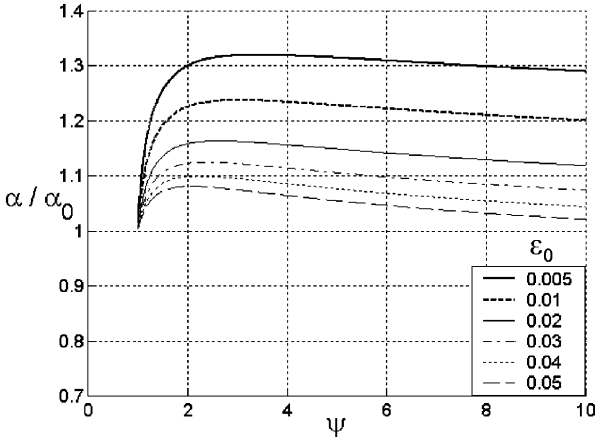

Fig. 3. Sharp initial transition followed by near constancy of cone edge wave speed, $c/c_0=\alpha/\alpha_0$, versus ratio of cone base radius to projectile radius, $\psi=r_c/r_p$, at several initial membrane strains, ε_0, resulting from various constant projectile velocities, V_p.

cases the cone edge wave speed jumps rapidly over the range $r_p < r_c < 1.5r_p$ (where the cone grows less than 50% of the projectile radius). The rise is almost complete at $r_c = 2r_p$ (i.e., growth by one projectile radius) and shortly thereafter it decreases extremely slowly, a result of the logarithmic factor in the denominator. Thus, after a brief transition region, c is virtually constant and the self-similar solution is justified up to the material strain limit. One feature to appreciate, however, is that eventually the logarithmic factor will reduce the cone-edge wave speed to zero as well as the membrane strain. Attempting to shrink the projectile to a point eliminates the length scale of the projectile tip and leads to a situation of no cone growth and infinite membrane strain at the projectile tip, as seen next. In the 1D model, however, the impact triangle or cone wave speed and strain are unaffected. These anomalies are at the heart of various difficulties discussed in Rakhmatulin and Dem'yanov (1961).

3.7. Strain distribution in the membrane and ground versus material coordinate perspectives

The tangential strain distribution in the membrane is easily found for both the curved cone region and the outer implosion wave region. From Eqs. (46) and (80) and strain continuity at the cone wave front, the strain throughout the fabric in material coordinates is simply

$$\varepsilon_t \approx \varepsilon_c r_c/r = \alpha^2 r_c/r, \quad r_p \leqslant r \leqslant a_0 t + r_p \tag{139}$$

The largest and crucial strain value is ε_p, the membrane strain at the projectile edge, which is

$$\varepsilon_p \approx \varepsilon_c r_c/r_p = \alpha^2 r_c/r_p \tag{140}$$

Note that the cone edge wave speed relative to ground is less than c since the edge is traveling in fabric material 'flowing' towards the projectile region of impact. This material added to the cone allows the cone to have a much larger angle without failure than it would have otherwise. The flow velocity is given by

$$\dot{u}_c/a_0 \approx \partial\tilde{u}(\zeta_c)/\partial s = \varepsilon_c\zeta_c(\ln\zeta_c - 1) = \alpha^2\zeta_c(\ln\zeta_c - 1) \tag{141}$$

and is negative. The velocity of the cone edge relative to ground is approximately $\tilde{c} \approx c + \dot{u}_c$ and substituting for $\zeta_c = r_c/s$ and manipulating the result we obtain

$$\tilde{c} \approx a_0\{\alpha + \alpha^2[1 + (1-\alpha)(r_c - r_p)/(\alpha r_c)][\ln\alpha - \ln(1 - (1-\alpha)r_p/r_c) - 1]\} \tag{142}$$

Typically $\tilde{c}$ is smaller than c by 10–20%. Fig. 2, illustrates this effect.

A consequence of the cone edge wave speed change in perspective is that the inverse smoothness of the strain ε_t in r occurs in material coordinates but is distorted in ground coordinates since the cone edge is actually significantly closer to the projectile. This sharpens the growth in strain approaching the projectile as well as increasing the local slope, a feature that can be seen in plots from simulations of biaxial fabric impact in Cunniff (1992).

In the 1D case, Eq. (55) indicates that the tape material behind the tensile wave flows towards the impact point with constant velocity $\dot{u}_1 = -\varepsilon_0 a_0$. The velocity of the triangle wave front relative to ground, denoted $\tilde{c}$, is given as the material coordinates value $c = \alpha_0 a_0$ times the 'stretch factor' $1 + \varepsilon_0 = 1 + \alpha_0^2$ (ignored in 2D) minus the flow velocity $\dot{u}_1$, i.e.,

$$\tilde{c} = \alpha_0 a_0(1 + \varepsilon_0) - \dot{u}_1 = \alpha_0 a_0(1 - \alpha_0 + \alpha_0^2) \tag{143}$$

to compare to $\tilde{c} \approx \alpha_0 a_0(1 - \alpha_0)$ in Eq. (142) for 2D, agreeing closely upon impact ($r_c \approx r_p$).

In the 1D case, the analysis that led to Eqs. (121) and (131) also shows that the cone or triangle deflection angle γ (relative to ground) is fixed and follows

$$\sin\gamma = V_p/\{(1 + \varepsilon_0)\alpha_0 a_0\} = V_p\Big/\left(a_0\sqrt{\varepsilon_0(1 + \varepsilon_0)}\right) \tag{144}$$

From this and Eq. (133) we get the useful approximations

$$\gamma \approx (2V_p/a_0)^{1/3} \tag{145}$$

and

$$\gamma \approx (4\varepsilon_0)^{1/4} \tag{146}$$

Both turn out to be surprisingly accurate for strains of interest in the paper.

As mentioned, the cone angle γ is fairly large due to the flow of material into the cone edge rather than due to the membrane strain. The 1D case is useful for illustrating that most of this angle comes from flow of material towards the impact zone. When the cone wave front has traveled from r_p to r_c in material coordinates, the unstretched length of material in the diagonal from the projectile edge to the wave front is $r_c - r_p$. The length change Δ_ε due to strain is

$$\Delta_\varepsilon = \varepsilon_0(r_c - r_p) = \varepsilon_0\alpha_0 a_0 t \tag{147}$$

On the other hand, the amount of material Δ_u that has been fed into triangle edge relative to ground can be shown to be the displacement

$$\Delta_u = u_1(r_c) = \varepsilon_0((1-\alpha_0)/\alpha_0)(r_c - r_p) = \varepsilon_0(1-\alpha_0)a_0 t \tag{148}$$

The ratio of the length change from strain to the total from both strain and flow is

$$\Delta_\varepsilon/(\Delta_u + \Delta_\varepsilon) = \alpha = \sqrt{\varepsilon_0/(1+\varepsilon_0)} \tag{149}$$

Typically $\varepsilon_{max} < 0.04$, so this ratio is at most 0.2 indicating only 20% of the length change to generate the large deflection angle, γ, comes from strain in the material; the other 80% is flow.

3.8. Behavioral features near threshold velocity for instantaneous perforation (no cone growth)

Note that the membrane stress grows substantially during the transition, so under steady projectile velocity conditions, a stress concentration will develop relative to constant stresses seen in 1D impact. From the perspective of impact velocity, the maximum possible to avoid *instant* perforation is given by the 1D solution as

$$V_{p,max} \approx a_0\sqrt{2}\alpha_{0\,max}^{3/2} \tag{150}$$

where $\alpha_{0\,max} \approx \sqrt{\varepsilon_0} = \sqrt{\varepsilon_{max}}$ is the maximum initial wave speed the membrane can tolerate without instant failure. However, for the cone edge to grow to just $r_c \approx 1.5r_p$ without perforation and noting that $\varepsilon_p = \alpha^2(r_c/r_p)$ at the projectile edge, the velocity $V_{p,max}$ must be lowered about 25%. This suggests that under deceleration from membrane reaction forces, the deceleration must be very high to avoid the stress concentration. This issue is taken up in more detail later.

In the above analysis, we have used several approximations: First, we have assumed no slip of the membrane in the region of contact with the projectile. However, slip may lower the strain development in the transition region as the tension wave travels both outward and inward from the projectile edge. Thus we would expect the strain buildup in this transition regime to be slightly delayed but complete, nevertheless, by the time the transition has passed.

Other perturbations are likely to result from the rapid increase in cone wave speed in the transition (relative to the assumed self-similar solution), but beyond this transition time we expect the fabric strain and wave shapes to quickly stabilize, especially in the important cone region. This will likely occur well before the cone wave front radius has become double the projectile radius. By this time the tension wave front radius will be an order of magnitude larger than both r_p and r_c. Another assumption was to use $\tilde{u}$ of Eq. (45) to represent the true displacement u. This may affect the strain and displacement nearer to the

tension wave front (where the $\beta = 1/2$ solution has by then largely decayed) but is unimportant back at the cone wave front where the cone and tension wave solutions were matched. In essence potential side effects of these approximations are serendipitously suppressed by the very fact that the strain starts at the 1D value but then rises sharply without overshoot. The exact details of the rise appear to matter little.

4. Deceleration of projectile and membrane strain evolution

We have assumed the projectile has finite mass M_p and initial contact with the membrane occurs within a circular a region of radius $r_p = D_p/2$, which has mass $m_p = \rho h \pi r_p^2$. Due to reaction forces from the membrane, the projectile velocity decreases in two stages. First is a virtually discontinuous drop from V_p just prior to impact to V_{p0} just after impact. The value of V_{p0} is determined later using conservation of momentum. From V_{p0}, projectile deceleration then occurs continuously over time $t > 0$. To avoid perforation, the projectile velocity must decrease fast enough to compensate for the tendency of the membrane strain ε_p to increase with cone base radius r_c, and furthermore, ε_p must be kept below ε_{max}, the membrane failure strain.

Though an exact analysis for varying projectile velocity is intractable, we can develop useful approximations using a simple adaptation of the present results to decreasing velocity. In 1D we will comment later on the validity of this approach and show that it gives accurate results. Calculating the deceleration of the projectile requires knowing the resisting force exerted by the membrane opposing projectile motion. This requires knowing the cone angle γ_p at the circle of contact with the projectile in ground coordinates. The angle γ was initially defined relative to ground, so we need $\gamma_p = \gamma(\xi_p)$.

As the projectile slows, the above analysis for constant projectile velocity may not give quite the correct cone geometry. We should note, however, certain beneficial factors such as the cone edge wave speed and projectile velocity being related roughly through $c \propto V^{2/3}$ after the initial transition. This means that local cone angles will change fairly slowly in V, roughly as $\gamma \propto V^{1/3}$, as we see in 1D. Thus the cone will tend to keep the constant velocity shape.

4.1. Local cone angle and reactive force on the projectile

From Eqs. (63) and (66) the local cone angle at the edge of the projectile is

$$\sin\gamma_p = -Y'(\xi_p)/R(\xi_p) \tag{151}$$

where from Eq. (79)

$$R(\xi) = 1 + \varepsilon_t(\xi) = 1 + \varepsilon_c/\xi + (1/2)(\varepsilon_c^2/\xi^2)(\xi - \xi^3) + \cdots \tag{152}$$

and from Eq. (93)

$$Y'(\xi) \approx -\kappa_1 \, e^{\varepsilon_c/\xi} = -\kappa_1\{1 + \varepsilon_c/\xi + (1/2)(\varepsilon_c^2/\xi^2) + \cdots\} \tag{153}$$

which is especially valid for $\xi_p \leqslant \xi < 0.8$. Taking $\xi = \xi_p$ and examining the ratio of the two, one sees to high accuracy that $\sin\gamma_p \approx -\kappa_1$ where the relative error is of order $\varepsilon_c^2/(2\xi_p^2)$ so is typically much less than 1%. By Eq. (112) for κ_1, we have

$$\sin\gamma_p \approx -\kappa_1 \approx \{V/(\alpha a_0)\}\{1 - \varepsilon_c[r_c/(r_c - r_p)]\ln(r_c/r_p)\} \tag{154}$$

We adapt Eq. (154) to decreasing velocity using instantaneous values for $c = \alpha a_0$.

The reactive force exerted by the membrane on the projectile is

$$F = -2\pi r_p E h \varepsilon_t(\xi_p)\sin\gamma_p = -2\pi r_p E h \varepsilon_c(r_c/r_p)\sin\gamma_p = -2\pi r_p E h \alpha^2 (r_c/r_p)\sin\gamma_p \tag{155}$$

where E and h are membrane modulus and thickness, respectively. Using Eq. (154) yields

$$F \approx -2\pi r_p E h \alpha (V/a_0)(r_c/r_p)\{1 - \alpha^2[r_c/(r_c - r_p)]\ln(r_c/r_p)\} \tag{156}$$

The second term in curly brackets is small, being less than $\varepsilon_p = \varepsilon_c/\xi_p$, the strain adjacent to the projectile, which is less than 0.05. Keeping only the dominant term in Eq. (156) and noting that

$$\alpha = (1/a_0)\,dr_c/dt \tag{157}$$

where $a_0^2 = E/\rho$ we obtain the important result

$$F \approx -(2\pi r_p^2 E h/a_0)(V/a_0)(r_c/r_p)\,d(r_c/r_p)/dt = -\pi r_p^2 \rho h V\,d(r_c/r_p)^2/dt \tag{158}$$

On the other hand, in 1D the reactive force is simply

$$F = 2\pi r_p h E \varepsilon \sin\gamma \approx 2\pi r_p h E \varepsilon \gamma \approx (\pi r_p h E/2)(2V/a_0)^{5/3} \tag{159}$$

using Eqs. (133), (145) and (146), and where the strain ε now changes with time. We also have

$$\gamma \approx \{(2F)/(\pi r_p E)\}^{1/5} \approx (4\varepsilon)^{1/4} \approx (2V/a_0)^{1/3} \tag{160}$$

which underscores that the angle γ is very *insensitive* to the force exerted on the projectile, the material strain, and even to the projectile velocity. Typically the longitudinal wave speed greatly exceeds both the speed of the growing triangle and the projectile velocity, i.e., $a_0 \gg c > V$. Thus, as the projectile velocity decreases, the configuration and distribution of material strain rapidly adjust, especially the crucial flow of material into the cone, $\dot{u}_1 = -a_0\varepsilon$. This justifies making the simple and direct adaptation of our constant velocity results to decreasing velocity.

Rakhmatulin and Dem'yanov (1961) discuss this issue but mainly in the case of non-linear stress–strain behavior following Ryabova (1953). Their main results are complicated expressions for differential changes in the position of the cone wave front, and tape stresses and strains there as well as at the projectile. At the end, they discuss the simplifications arising from assuming elastic behavior, but the results remain complicated. However, once we invoke the condition $a_0 \gg c > V$, the complicating terms all vanish, leading us to our starting point.

4.2. Areal density ratio, momentum exchange and velocity evolution during and after impact

We recall that $m_p = \rho h A_p = \rho h \pi r_p^2$ is the membrane mass in contact with the projectile. The total mass the membrane reactive force must decelerate is thus

$$M_0 = M_p + m_p \tag{161}$$

We let Γ_0 be the areal density ratio of the membrane to the projectile, which is

$$\Gamma_0 = m_p/M_p = \rho h A_p/M_p = \rho h \pi r_p^2/M_p \tag{162}$$

We assume the projectile velocity, V_p, before impact and velocity, V_{p0}, immediately after impact are related by simple momentum exchange (see for example Fatt et al. (2003) for blunt impact into fiber–metal laminates). Thus

$$V_{p0} = V_p/(1 + \Gamma_0) \tag{163}$$

Since $F = -M_0\,dV/dt$, Eq. (158) yields

$$M_0\,dV/dt = -\pi r_p^2 \rho h V\,d(r_c/r_p)^2/dt \tag{164}$$

or

$$\mathrm{d}V/V = -[\Gamma_0/(1+\Gamma_0)]\,\mathrm{d}(r_c/r_p)^2 \tag{165}$$

Letting $\psi = r_c/r_p$ and noting that $r_c = r_p$ and $V = V_{p0}$ just after impact, Eq. (165) integrates to the important result

$$V/V_p = V/\{V_{p0}(1+\Gamma_0)\} = \{1/(1+\Gamma_0)\}\exp\{-[\Gamma_0/(1+\Gamma_0)](\psi^2-1)\} \tag{166}$$

In the 1D case, letting F_{p0} be the initial (right after momentum exchange at impact) projectile deceleration force, Eq. (159) relating deceleration force and velocity can be written as

$$F/F_{p0} = (V/V_{p0})^{5/3} \tag{167}$$

where

$$F_{p0} \approx (\pi r_p h E/2)(2V_{p0}/a_0)^{5/3} \tag{168}$$

This deceleration force acts on M_0, the projectile mass plus the mass of the membrane material it has just contacted. Thus

$$M_0\,\mathrm{d}V/\mathrm{d}t = -F \tag{169}$$

and using $V = \mathrm{d}\delta/\mathrm{d}t$ where δ is distance traveled by the projectile after impact and using Eq. (167) we write this as

$$M_0 V_{p0}^2 (V/V_{p0})^{-2/3}\mathrm{d}(V/V_{p0}) = -F_{p0}\,\mathrm{d}\delta \tag{170}$$

Upon integration we obtain

$$(V/V_{p0})^{1/3} = 1 - (F_{p0}\delta)/(3M_0V_{p0}^2) \tag{171}$$

Letting δ_{p0} be the distance for the projectile to stop ($V = 0$), Eqs. (168) and (171) yield

$$\delta_{p0} = [3M_0/(2\pi r_p h\rho)](2V_{p0}/a_0)^{1/3} \tag{172}$$

Also, letting

$$\varepsilon_{p0} = \alpha_{p0}^2 \approx \{V_{p0}/(\sqrt{2}a_0)\}^{4/3} = \{V_p/[\sqrt{2}a_0(1+\Gamma_0)]\}^{4/3} \tag{173}$$

(actually an approximation) and recalling Eqs. (159), (160), (169), (170) and (171) we find

$$(F/F_{p0})^{1/5} \approx (\varepsilon/\varepsilon_{p0})^{1/4} \approx (V/V_{p0})^{1/3} \approx 1 - \delta/\delta_{p0} \approx 1\Big/\sqrt{1+t/t_{p0}} \tag{174}$$

where

$$t_{p0} \equiv \delta_{p0}/(2V_{p0}) = \{3M_0/(2\pi r_p h\rho a_0)\}\{a_0/(2V_{p0})\}^{2/3} \tag{175}$$

is a characteristic time of deceleration, being half the time it would take the unrestrained projectile to travel distance δ_{p0}.

In 1D, we note for small times that $F/F_{p0} \approx 1 - (5/2)t/t_{p0}$ so although decreasing rapidly even after momentum exchange occurs, the force drops linearly at small times. Also Eq. (174) shows that while the projectile stops in a finite distance, δ_{p0}, the time it takes to stop completely is theoretically infinite (though in practice it is truncated by boundary effects).

4.3. 2D membrane strain evolution and maximum strain concentration adjacent to the projectile

In the membrane next to the projectile just after impact at $t = 0^+$, we have $\varepsilon_{p0} = \alpha_{p0}^2 \approx \{V_p/[\sqrt{2}a_0(1+\Gamma_0)]\}^{4/3}$, and thus, Eq. (135), becomes

$$V/V_{p0} \approx (\alpha/\alpha_{p0})^{3/2}\sqrt{\psi \ln\{1+(1/\alpha)(\psi-1)\}/\{(1/\alpha)(\psi-1)\}} \tag{176}$$

where $\psi = r_c/r_p$. Since

$$\alpha/\alpha_{p0} = \sqrt{(1/\psi)(\varepsilon_p/\varepsilon_{p0})} \tag{177}$$

we can use Eq. (166) to rearrange the above expression to yield

$$\varepsilon_p/\varepsilon_{p0} \approx \exp\{-[4\Gamma_0/(3(1+\Gamma_0))](\psi^2-1)\}\psi^{1/3}[(1/\alpha)(\psi-1)/\ln\{1+(1/\alpha)(\psi-1)\}]^{2/3} \tag{178}$$

Given $V_{p0} = V_p/(1+\Gamma_0)$, this expression allows us to calculate the evolution of the strain enhancement ratio, $\varepsilon_p/\varepsilon_{p0}$, versus the cone growth ratio, $\psi = r_c/r_p$ (though to use it one must calculate α for each V and ψ combination using the above expression for V/V_{p0}).

Due to the decaying exponential, the strain peaks and we would like to determine the threshold velocity for perforation, i.e., the maximum velocity $V_{p0} = V_p/(1+\Gamma_0)$ that still keeps the membrane strain below the failure threshold. Thus we let $K = \varepsilon_p/\varepsilon_{p0}$ be the strain amplification factor in the membrane at the projectile edge in the time period after impact. Additionally we recall $\alpha = \sqrt{\varepsilon_c} = \sqrt{\varepsilon_p/\psi}$. Thus Eq. (178) becomes

$$K = \frac{\varepsilon_p}{\varepsilon_{p0}} \approx \exp\left\{-\frac{4\Gamma_0}{3(1+\Gamma_0)}[\psi^2-1]\right\}\psi^{1/3}\left[\frac{\sqrt{\psi/\varepsilon_p}(\psi-1)}{\ln\{1+\sqrt{\psi/\varepsilon_p}(\psi-1)\}}\right]^{2/3} \tag{179}$$

where $\varepsilon_p = \psi\alpha^2(V,\psi)$ and $V = V(V_{p0},\Gamma_0)$ can be obtained from Eqs. (166), (176)–(178).

In 1D we can use Eq. (174) to show that

$$K = \frac{\varepsilon_p}{\varepsilon_{p0}} \approx \exp\left\{-\frac{4\Gamma_0}{3(1+\Gamma_0)}[\psi^2-1]\right\} \tag{180}$$

Thus the maximum value in 1D is automatically $K_{max} = 1$, which occurs just after impact.

Returning to 2D, the maximum value, K_{max}, requires the strain constraint $\varepsilon_p \leqslant \varepsilon_{max}$ as ψ grows. The decay rate of the exponential overwhelmingly dominates the peak behavior, so the value ψ_{max}, where the maximum in ψ occurs, is easy to approximate when $\psi_{max} \gg 1$, but the result works even for ψ_{max} near 1. The logarithmic term is slowly varying, and we can replace $\psi - 1$ by ψ in seeking an approximate maximum. Also K reaching K_{max} implies that ε_p reaches ε_{max} and is stationary on the right-hand side (zero derivative in ψ). Raising both sides of Eq. (179) to the power 3/4 and taking derivatives with respect to ψ^2 with $\varepsilon_p = \varepsilon_{max}$ yields

$$\psi_{max} \approx \sqrt{(1+\Gamma_0)/(2\Gamma_0)} \tag{181}$$

and thus

$$K_{max} \approx \exp\left\{-\frac{4\Gamma_0}{3(1+\Gamma_0)}(\psi_{max}^2-1)\right\}\psi_{max}^{1/3}\left[\frac{\sqrt{\psi_{max}/\varepsilon_{max}}(\psi_{max}-1)}{\ln\{1+\sqrt{\psi_{max}/\varepsilon_{max}}(\psi_{max}-1)\}}\right]^{2/3} \tag{182}$$

Note that $K_{max} = 1$ for $\Gamma_0 \geqslant 1$ so there is no strain concentration, and $\psi_{max} = r_c/r_p = 1$, as it should. Note that ψ_{max} and K_{max} both increase as Γ_0 decreases and the strain concentration plays an increasing role. However, the cone base size required to lower the V_{p0} velocity to $V_{final} = 0.02V_{p0}$ (i.e. 2% residual velocity) is easy to determine. From Eq. (166) we have

$$\psi_{final} = r_{c,final}/r_p = \sqrt{1+\ln(50)(1+\Gamma_0)/\Gamma_0} \tag{183}$$

For example for $\Gamma_0 = 0.125$, we find $\psi_{final} = r_{c,final}/r_p \approx 6.02$, almost three times the growth to achieve maximum strain. This result is fairly insensitive V_{final}.

4.4. Distance required to stop the projectile for the 2D membrane

In Fig. 3 we saw that, under constant projectile velocity, the cone edge velocity $c = \alpha a_0$ is almost constant after a very brief transition period of growth in $\psi = r_c/r_p$ where it jumps a few percent above the starting 1D value. Based on Eq. (129) we have the approximation

$$c = r_p \, d\psi/dt \approx 1.23 a_0 \{V/(a_0\sqrt{2})\}^{2/3} \tag{184}$$

This allows us to calculate the membrane deflection, δ, versus ψ and also δ_{p0}, the deflection when the projectile stops. We can then use Eq. (166) to obtain δ versus $\psi = r_c/r_p$ and we obtain

$$\begin{aligned}\delta(\psi) &= \int_1^{\psi} \frac{V}{dw/dt} dw = \int_1^{\psi} \left(r_p V \Big/ \left[1.23 a_0 \left\{ V \Big/ \left(a_0\sqrt{2} \right) \right\}^{2/3} \right] \right) dw \\ &= \left(\frac{1}{1.23} \right) (2V_{p0}/a_0)^{1/3} r_p \, e^{\frac{\Gamma_0}{3(1+\Gamma_0)}} \int_1^{\psi} e^{-\left(\frac{\Gamma_0}{3(1+\Gamma_0)} \right) w^2} dw \end{aligned} \tag{185}$$

Note that

$$\int_1^{\psi} e^{-\left(\frac{\Gamma_0}{3(1+\Gamma_0)} \right) w^2} dw = \frac{\sqrt{\pi}}{2} \sqrt{\frac{3(1+\Gamma_0)}{\Gamma_0}} \left\{ \operatorname{erf}\left(\psi \sqrt{\frac{\Gamma_0}{3(1+\Gamma_0)}} \right) - \operatorname{erf}\left(\sqrt{\frac{\Gamma_0}{3(1+\Gamma_0)}} \right) \right\} \tag{186}$$

We see that $\delta \to \delta_{p0}$ as $\psi \to \infty$ and Eq. (186) becomes

$$\int_1^{\infty} e^{-\left(\frac{\Gamma_0}{3(1+\Gamma_0)} \right) w^2} dw = \sqrt{3\pi(1+\Gamma_0)/(4\Gamma_0)} \left\{ 1 - \operatorname{erf}\left(\sqrt{\Gamma_0/[3(1+\Gamma_0)]} \right) \right\} \tag{187}$$

Thus

$$\frac{\delta_{p0}}{r_p} \approx \frac{1}{1.23} \left(\frac{2V_{p0}}{a_0} \right)^{1/3} e^{\frac{\Gamma_0}{3(1+\Gamma_0)}} \sqrt{\frac{3\pi(1+\Gamma_0)}{4\Gamma_0}} \left\{ 1 - \operatorname{erf}\left(\sqrt{\frac{\Gamma_0}{3(1+\Gamma_0)}} \right) \right\} \tag{188}$$

Recalling $V_{p0} = V_p/(1+\Gamma_0)$ and expanding the exponential and error function we finally have

$$\frac{\delta_{p0}}{r_p} \approx 1.25 \left\{ \frac{(1+4\Gamma_0/3)}{(1+\Gamma_0)^{5/6}} \right\} \left(\frac{1}{\sqrt{\Gamma_0}} \right) \left\{ 1 - \sqrt{\frac{\Gamma_0}{3(1+\Gamma_0)}} \right\} \left(\frac{2V_p}{a_0} \right)^{1/3} \tag{189}$$

In 1D we obtained Eq. (172) and using Eqs. (161)–(163) this becomes.

$$\frac{\delta_{p0}}{r_p} \approx \frac{3}{2} \left\{ \frac{(1+\Gamma_0)^{2/3}}{\Gamma_0} \right\} \left(\frac{2V_p}{a_0} \right)^{1/3} \tag{190}$$

to compare to Eq. (189) for the 2D membrane. Note that at small Γ_0 the two results diverge with the 1D result growing relative to the 2D membrane result as $\sqrt{\Gamma_0}$.

4.5. Energy absorbed in stopping projectile and V_{50} limit

Next we consider the energy absorbed by the membrane in stopping the projectile from velocity V_{p0}. At this point, the kinetic energy of the projectile plus membrane patch it contacts is

$$\vec{E}_{p0} = M_0 V_{p0}^2/2 \tag{191}$$

and this equals the work done by the membrane. The 1D case is easy and by Eq. (174) we have

$$\int_0^{\delta_{p0}} F(\delta)\,\mathrm{d}\delta = F_{p0}\int_0^{\delta_{p0}} (1-\delta/\delta_{p0})^5\,\mathrm{d}\delta = F_{p0}\delta_{p0}/6 \tag{192}$$

so that

$$\vec{E}_{p0} = F_{p0}\delta_{p0}/6 \tag{193}$$

From Eqs. (168) and (173) we have

$$F_{p0} \approx 2^{3/2}\pi r_p h E\varepsilon_{p0}^{5/4} = 2^{3/2}\pi r_p h\sigma_{p0}^{5/4}/E^{1/4} \tag{194}$$

where $\sigma_{p0} = E\varepsilon_{p0}$ after momentum exchange at impact. Combining Eqs. (162) and (172) yields

$$\delta_{p0} = 3r_p\{(1+\Gamma_0)/\Gamma_0\}(2V_{p0}/a_0)^{1/3} = 3r_p\{(1+\Gamma_0)/\Gamma_0\}(4\varepsilon_{p0})^{1/4} \tag{195}$$

Thus from Eqs. (191) and (193)–(195) we arrive at

$$M_0V_{p0}^2/2 = (M_0/\rho)\sigma_{p0}\varepsilon_{p0}^{1/2} = M_0a_0^2\varepsilon_{p0}^{3/2} \tag{196}$$

We can also rewrite this projectile energy equation in terms of Γ_0, and using Eq. (162) we get

$$M_0V_{p0}^2/2 = \{(1+\Gamma_0)/\Gamma_0\}A_p h\sigma_{p0}\varepsilon_{p0}^{1/2} = \{(1+\Gamma_0)/\Gamma_0\}A_p h\rho a_0^2\varepsilon_{p0}^{3/2} \tag{197}$$

By convention V_{50} is the threshold projectile velocity V_p above which the membrane fails by perforation 50% of the time. Using Eq. (163) in Eq. (197), taking V_p as V_{50} and replacing σ_{p0} and ε_{p0} by the limiting values σ_{max} and ε_{max}, respectively, results in

$$M_pV_{50}^2/2 = \{(1+\Gamma_0)^2/\Gamma_0\}A_p h\sigma_{max}\varepsilon_{max}^{1/2} = (1+\Gamma_0)^2M_pa_0^2\varepsilon_{max}^{3/2} \tag{198}$$

and

$$V_{50} = (1+\Gamma_0)\sqrt{(2A_p h\sigma_{max})/(M_p\Gamma_0)}\,\varepsilon_{max}^{1/4} = \sqrt{2}(1+\Gamma_0)a_0\varepsilon_{max}^{3/4} \tag{199}$$

Note that the last equation follows directly from Eq. (173). Also, Eq. (198) should not be interpreted as an energy balance equation per se, but as a relationship between maximum projectile energy without failure, and various projectile and tape properties. Clearly the V_{50} velocity is influenced by the size of the contact zone through the Γ_0.

In 2D, the energy calculation is somewhat more complicated to obtain directly, but Eq. (173) together with acknowledgement of the strain concentration K_{max} of Eq. (182) results in

$$V_{50} = \sqrt{2}(1+\Gamma_0)a_0(\varepsilon_{max}/K_{max})^{3/4} \tag{200}$$

where we see that $K_{max} = K_{max}(\Gamma_0, \varepsilon_{max})$ through Eqs. (181) and (182). We will convert this equation into convenient dimensionless form to compare with published experimental results.

4.6. Residual velocity in case of perforation ($V_p > V_{50}$)

To avoid perforation, the strain ε_p at the projectile radius must be kept below ε_{max}, which implies a limiting value for V_p, known as V_{50} in the literature. For $V_p > V_{50}$, perforation will occur but the projectile velocity, V_{res}, will be less than V_p. Due to momentum exchange (assuming a plug of membrane of area roughly A_p is cut out and travels with the projectile) one might expect $V_{res} \approx V_{p0} = V_p/(1+\Gamma_0)$ as the 1D model clearly predicts. However, perforation is not instantaneous as some cone growth may occur, depending on Γ_0, and V_p, and membrane reactive forces decelerate the projectile below that due to momentum

transfer alone. Assuming $V_p > V_{50}$ we let ψ_{fail} be the value of ψ when the strain limit is first exceeded, and note that

$$1 < \psi_{fail} \leqslant \psi_{max} \approx \sqrt{(1+\Gamma_0)/(2\Gamma_0)} \tag{201}$$

We can combine $V_{p0} = V_p/(1+\Gamma_0)$ with Eq. (166) and write

$$V_{res}/V_p = \{1/(1+\Gamma_0)\}\exp\{-(\psi_{fail}^2 - 1)\Gamma_0/(1+\Gamma_0)\} \tag{202}$$

Note that for $V_p = V_{50}^+$, i.e., just above the perforation threshold, Eqs. (166) and (201) yield

$$V_{res}/V_{50}^+ = \{1/(1+\Gamma_0)\}\exp\{\Gamma_0/(1+\Gamma_0) - 1/2\} \tag{203}$$

(For $\Gamma_0 > 1$ the exponential becomes 1.) The exponential has an appreciable effect for small Γ_0. Also as V_p increases above V_{50}, ψ_{fail} decreases below ψ_{max}, and $V_{res} \to V_p/(1+\Gamma_0)$ by Eq. (202). This is seen as curvature in plots of V_{res} versus $V_p \geqslant V_{50}^+$. Later we will generate plots of Eq. (202) based on numerically solving for ψ_{fail}. The equation to solve is based on Eq. (179), with $\varepsilon_{p0} = \alpha_{p0}^2$ given by Eq. (173) and setting $\varepsilon_p = \varepsilon_{max}$. The equation is then

$$2\left(\frac{a_0}{V_p}\right)^2 \approx \left(\frac{\psi_{max}}{2\Gamma_0\varepsilon_{max}}\right)^2 \psi_{max}^2 \exp\left\{-\frac{1}{\psi_{max}^2}[\psi_{fail}^2 - 1]\right\} \frac{\psi_{fail}(\psi_{fail}-1)}{\ln\left\{1+\sqrt{\psi_{fail}/\varepsilon_{max}}(\psi_{fail}-1)\right\}} \tag{204}$$

5. Application to impact response of balanced fabric

We apply the model to the impact response of a balanced fabric (e.g., a plain weave) or several layers thereof with the same yarn orientation. Details such as crimp angle, yarn denier and number of yarns per unit width or length are ignored as is the directional behavior or orthotropy in mechanical properties with respect to the yarn axes. Our hypothesis is that the dimensionality 2D is the primary factor in fabric response and that no adaptation of the 1D model as, say, four material spokes representing the yarn directions will work despite the fact that the tension waves will travel with great preference along the yarn axes.

We also define an effective diameter of impact $D_{p\theta} = \theta D_p$, and area $A_{p\theta} = \theta^2 A_p$, where θ is a parameter typically somewhat greater than unity. The idea is that due to such factors as fabric wraparound effects, projectile nose plastic deformation and perhaps tearing roughness caused by the square nature of the fabric, and causing an expanded plug of fabric in the initial momentum exchange in thick systems, the effective fabric mass in contact with the projectile is

$$m_{p\theta} = \theta^2 m_p = \rho_f h_f A_{p\theta} \tag{205}$$

where we add the subscript "f" to refer to fabric effective properties (i.e., h_f is the effective thickness of fabric or fiber material with the voids ignored or removed and ρ_f is the fabric and fiber density). We also define a revised areal density ratio as

$$\Gamma_{0\theta} = m_{p\theta}/M_p = \theta^2(m_p/M_p) = \theta^2\Gamma_0 \tag{206}$$

where $\Gamma_0 = m_{p0}/M_p$ remains as the nominal value used to in reporting standardized experiments.

We distinguish yarn (or fiber) properties with the subscript "y" in addition to fabric (membrane) properties with the subscript "f". The effective modulus of the fabric is $E_f = E_y/2$ (since crossing yarns add cross-sectional area but not load carrying), but the fabric and yarn densities are the same, i.e., $\rho_f = \rho_y$. The failure strains are also equal, $\varepsilon_{f\,max} = \varepsilon_{y\,max}$, but the fabric failure stress is halved, i.e., $\sigma_{f\,max} = \sigma_{y\,max}/2$ compared to a yarn (fiber). The longitudinal wave speed for the fabric (along principal yarn directions) is

$$a_{0f} = \sqrt{E_f/\rho_f} = \sqrt{(E_y/2)/\rho_y} = a_{0y}/\sqrt{2} \tag{207}$$

being smaller than a_{0y} for a yarn because of the added mass of crossing yarns. Henceforth a_{0f} will refer to membrane or fabric tensile wave speed since both are modeled as a continuum.

5.1. V_{50} velocity in terms of Cunniff's dimensionless scaling parameters

We recall Eq. (200), and in view of the notational discussion above rewrite it as

$$V_{50} = (1 + \theta^2\Gamma_0)a_{0y}[\varepsilon_{y\max}/K_{\max}(\theta^2\Gamma, \varepsilon_{y\max})]^{3/4} \tag{208}$$

To reduce ballistic data for various fabrics to fit one curve Cunniff (1999c), defined two dimensionless variables, Γ_0 and Π as follows: Γ_0 is given by Eq. (206) and Π is given by

$$\Pi = V_{50}/\sqrt[3]{\Omega} \tag{209}$$

where $\sqrt[3]{\Omega}$ is a normalizing velocity and Ω is expressed in yarn (fiber) properties and is

$$\Omega = (1/2)(\sigma_{y\max}\varepsilon_{y\max}/\rho_y)\sqrt{E_y/\rho_y} = (1/2)\varepsilon_{y\max}^2 a_{0y}^3 \tag{210}$$

Note that Ω is the product of the elastic energy storage capability of the fiber per unit mass times the fibers tensile wave speed. Cunniff has argued for a relationship of the form

$$\Pi = f(\Gamma_0) \tag{211}$$

where f was said to be an increasing function of Γ_0 only, and was graphed empirically from data. Comparing Cunniff's empirical relationship with Eq. (208) in view of Eqs. (209) and (210) requires that $f(\Gamma_0)$ actually be

$$f(\theta^2\Gamma_0, \varepsilon_{y\max}) \equiv 2^{1/3}\varepsilon_{y\max}^{1/12}(1 + \theta^2\Gamma_0)/[K_{\max}(\theta^2\Gamma_0, \varepsilon_{y\max})]^{3/4} \tag{212}$$

with $K_{\max}(\theta^2\Gamma_0, \varepsilon_{y\max})$ as in Eq. (182) with Γ_0 in Eqs. (181) and (182) replaced by $\Gamma_{0\theta} = \theta^2\Gamma_0$ and $\varepsilon_{\max}$ replaced by $\varepsilon_{y\max}$. (To give better accuracy, $K_{\max}$ can be obtained numerically using Eq. (179)). This correspondence requires that the dependency on $\varepsilon_{y\max}$ be weak and the variation in θ among fabric systems be small. This proves to be true as we find later, as θ ranges between 1.25 and 1.35.

Explicitly, our version of $\Pi = f(\Gamma_0)$ is thus

$$V_{50}/\sqrt[3]{\Omega} = 2^{1/3}\varepsilon_{y\max}^{1/12}(1 + \theta^2\Gamma_0)/K_{\max}^{3/4} \tag{213}$$

where $K_{\max}$ is accurately represented by

$$K_{\max} \approx \exp\left\{ -\frac{4\theta^2\Gamma_0}{3(1+\theta^2\Gamma_0)}(\psi_{\max}^2 - 1)\right\}\psi_{\max}^{1/3}\left\{\frac{\sqrt{\psi_{\max}/\varepsilon_{y\max}}(\psi_{\max}-1)}{\ln[1+\sqrt{\psi_{\max}/\varepsilon_{y\max}}(\psi_{\max}-1)]}\right\}^{2/3} \tag{214}$$

and

$$\psi_{\max} \approx \sqrt{(1+\theta^2\Gamma_0)/(2\theta^2\Gamma_0)} \tag{215}$$

Note that the stain on impact, ε_{p0}, is typically well below the maximum, $\varepsilon_{y\max}$, and is given by

$$\varepsilon_{p0} = \alpha_{p0}^2 \approx \{V_{p0}/(\sqrt{2}a_{0y})\}^{4/3} = \{V_p/[\sqrt{2}a_{0y}(1+\theta^2\Gamma_0)]\}^{4/3} \tag{216}$$

The distance to stop the projectile becomes

$$\frac{\delta_{p0}}{r_p} \approx 1.25\left\{\frac{(1+4\theta^2\Gamma_0/3)}{(1+\theta^2\Gamma_0)^{5/6}}\right\}\left(\frac{1}{\sqrt{\theta^2\Gamma_0}}\right)\left\{1-\sqrt{\frac{\theta^2\Gamma_0}{3(1+\theta^2\Gamma_0)}}\right\}\left(\frac{2V_p}{a_{0y}}\right)^{1/3} \tag{217}$$

Comparing our result, Eq. (213), with Cunniff's empirical observations, Eq. (211), dependence is not only on Γ_0 and θ, but also mildly on $\varepsilon_{y\max}$, which is dimensionless. As a key factor in $f(\theta^2\Gamma_0, \varepsilon_{y\max})$, note that $2^{1/3}\varepsilon_{y\max}^{1/12} \approx 0.981$ for the typical value $\varepsilon_{y\max} \approx 0.04$. This outcome is insensitive to $\varepsilon_{y\max}$, so dependence on strain will mainly be through $K_{\max}$. In the next section we compare this result with Cunniff's plotted data for various multi-ply fabric systems of the best current materials technology.

Values of $\Gamma_0 > 0.2$ typically correspond the fabric depth being greater than the projectile length or diameter. This is seen by taking the projectile volume and density as $A_p h_p$ and ρ_p, respectively, where h_p is the projectile height and ρ_p is its density, so that

$$h_f = h_p(\rho_p/\rho_y)\Gamma_{0\theta} \tag{218}$$

Typically the projectile density exceeds that of the fiber by a factor of 5–10, and $\Gamma_0 > 0.2$ corresponds to a fabric with many plies (e.g., more than 20).

6. Discussion of results and comparison to experiments in the literature

We discuss some features of the model and briefly compare our predictions with experimental results in the literature. We also comment on additional results in 1D regarding membrane energy distribution, heat generation and momentum transfer, thus demonstrating model consistency.

6.1. Stress concentration effects and cone growth behavior versus areal density ratio

Fig. 4 shows plots of the strain concentration, K, versus normalized cone base radius, $\psi = r_c/r_p$, as calculated from Eq. (179) with $\theta^2\Gamma_0$ replacing Γ_0. Fig. 4a is for $\Gamma_0 = 0.125$ and Fig. 4b for $\Gamma_0 = 0.02$, and both are for $\theta = 1.30$ (as becomes important shortly) and for various values of the strain on impact, $0 < \varepsilon_{p0} \leqslant 0.05$, as given by Eq. (216). Also plotted is K for 1D given by Eq. (180) with $\theta^2\Gamma_0$ replacing Γ_0. The peak locations, $\psi_{\max}$, agree closely with those estimated from Eq. (215). Thus Eqs. (214) and (215) provide a very accurate estimate of $K_{\max}$, which decreases modestly as ε_{p0} increases. This may seem to favor

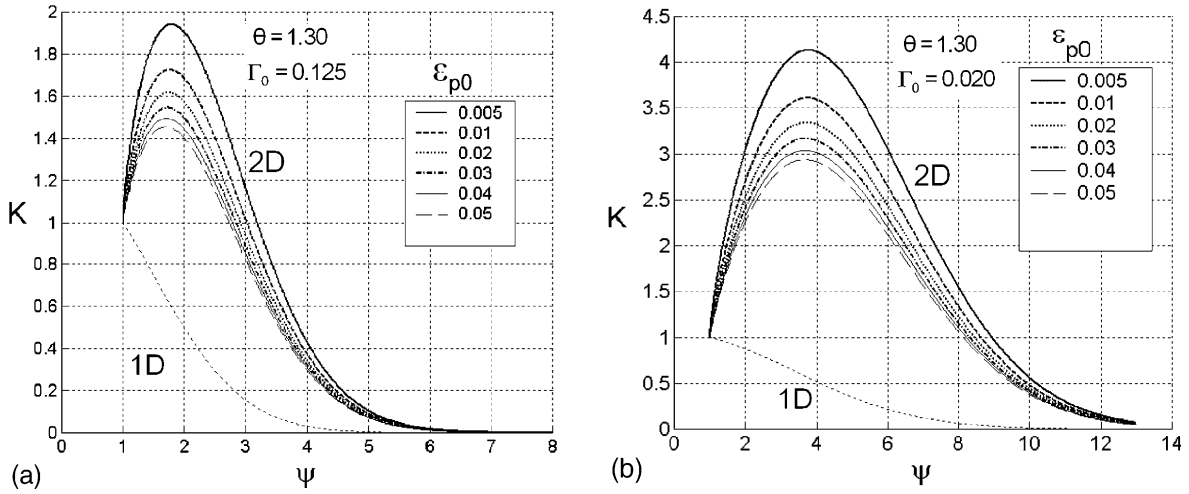

Fig. 4. Plots of the strain concentration, K, versus normalized cone base radius, $\psi = r_c/r_p$ for (a) $\Gamma_0 = 0.125$ and (b) $\Gamma_0 = 0.02$ and $\theta = 1.3$, and for various values of the membrane strain on impact, ε_{p0}, related to the initial velocity, V_p, by Eq. (216). Also shown are K results from 1D based on Eq. (180) with $\theta^2\Gamma_0$ replacing Γ_0.

high strain-to-failure materials, except that ε_{p0} increases as a_0 decreases due to the corresponding decrease in tensile stiffness.

Note, in Fig. 4a, that the normalized cone base radius, ψ, grows considerably (and is unbounded) *after* K reaches its peak value at $\psi = \psi_{max}$. This is not the case for the normalized maximum deflection, δ_{p0}/r_p, given by Eq. (217), which requires $\psi \to \infty$. For the strain to drop back to its initial value, ε_{p0}, we need $\psi \approx 2\psi_{max}$ and another doubling to reduce it to near zero. Note, however, that the normalized deflection, δ_{p0}/r_p is 1.8, or roughly ψ_{max}, but ψ itself will grow much higher as δ_{p0}/r_p is approached.

For the case of $\Gamma_0 = 0.02$ and $\theta = 1.30$ in Fig. 4b, corresponding to a much thinner membrane, δ_{p0}/r_p is about 3.9, i.e., more than double that for $\Gamma_0 = 0.125$, as they both scale roughly as $1/\sqrt{\theta^2\Gamma_0}$. (Similar scaling was proposed by Walker (1999).) Another doubling in ψ is necessary to bring the strain down to its initial value, ε_{p0}. Again Eq. (215) gives a good estimate, 3.9, of ψ_{max}, so Eqs. (214) and (215) provide a very accurate estimate of K_{max}, whose values are more than double those for $\Gamma_0 = 0.125$ in Fig. 4a.

This raises a crucial issue in experiments, namely, boundary effects that might occur in testing fabric systems at $\Gamma_0 = 0.02$, which may correspond to one or two fabric plies. Then δ_{p0} and ψ_{max} would be about 2 times the projectile diameter, or about 1 cm, though high strains persist for much larger ψ. On the other hand, the tensile wave speed, a_{0f}, is of order 10 times the cone edge wave speed, $\tilde{c}_f$, so the tension wave will have traveled of order 10 cm, which approaches the aperture boundary of many sample holders that clamp the fabric at the edges.

Thus it is possible for tension wave reflections from clamped boundaries to slow the inflow of membrane material from the implosion, thus influencing the response after the peak in Fig. 4b, possibly causing a second, higher strain peak, and thus, lowering the V_{50} response. This is exactly what is shown in Cunniff (1992) for single ply tests, where apertures of 10 cm cause significant reductions in V_{50} compared to 20 cm, and apertures of 2.5 cm cause V_{50} to drop by a factor of two. As expected, the residual velocities converge at higher impact velocities.

The same phenomenon is also apparent in experiments in Lim et al. (2003) for a single-ply, 12 cm × 12 cm Twaron® fabric specimen clamped along two opposite edges and impacted at $V_p = 206$ m/s by a spherical indentor. The V_{50} velocity of a large fabric sheet probably exceeds 206 m/s, yet V_{50} for these specimens was 130 m/s. The cone wave nears the boundary before significant penetration at 50 μs, enough time for about three full reflections of the tension wave.

This begs the question as to the exact purpose of rigid clamping (apart from limiting specimen damage from subsequent impact with equipment). In practice, clamp slip is difficult to avoid, and in body armor clamping is not practical. Theoretically it confuses interpretation of results for purposes of modeling larger systems such as body armor, and inadvertently it puts to a disadvantage materials such as Spectra® that have the highest wave-speeds, a_{0f}.

6.2. Comparison of model predictions to master curve data reductions of Cunniff

Fig. 5 shows our Π versus Γ_0 result, Eq. (213), graphed on figures of plotted experimental data by Cunniff (1999c). Results are shown for Kevlar® 29, Kevlar KM2, PBO and Spectra® 1000 fabric systems, respectively. We have removed Cunniff's empirically drawn curves and replaced them with Eq. (213) for the θ values shown (though the lines follow virtually the same paths as Cunniff's). The values for all fiber properties are Cunniff's, as are the normalizing velocities, $\sqrt[3]{\Omega}$ (i.e., his $\sqrt[3]{U^*}$). In Fig. 5a, for instance for Kevlar® 29, $\sigma_{y\,max} \approx 2.9$ GPa, $\varepsilon_{y\,max} \approx 0.034$, $E_y \approx 74$ GPa and $\rho_y = 1440$ kg/m^3 producing the normalizing velocity $\sqrt[3]{\Omega} \approx 624$ m/s using Eq. (210). In the case of Spectra® 1000 in Fig. 5d the data was plotted using Cunniff's 20% reduction in $\sqrt[3]{\Omega}$ needed for good agreement. Cunniff suggests this anomaly is the result of thermal softening and we agree, as discussed later.

In Fig. 5 a–d, the only parameter we could adjust was the effective contact diameter factor θ in θD_p and even then the range $1.25 \leqslant \theta \leqslant 1.35$ is remarkably narrow. The effective increase in projectile nose diameter

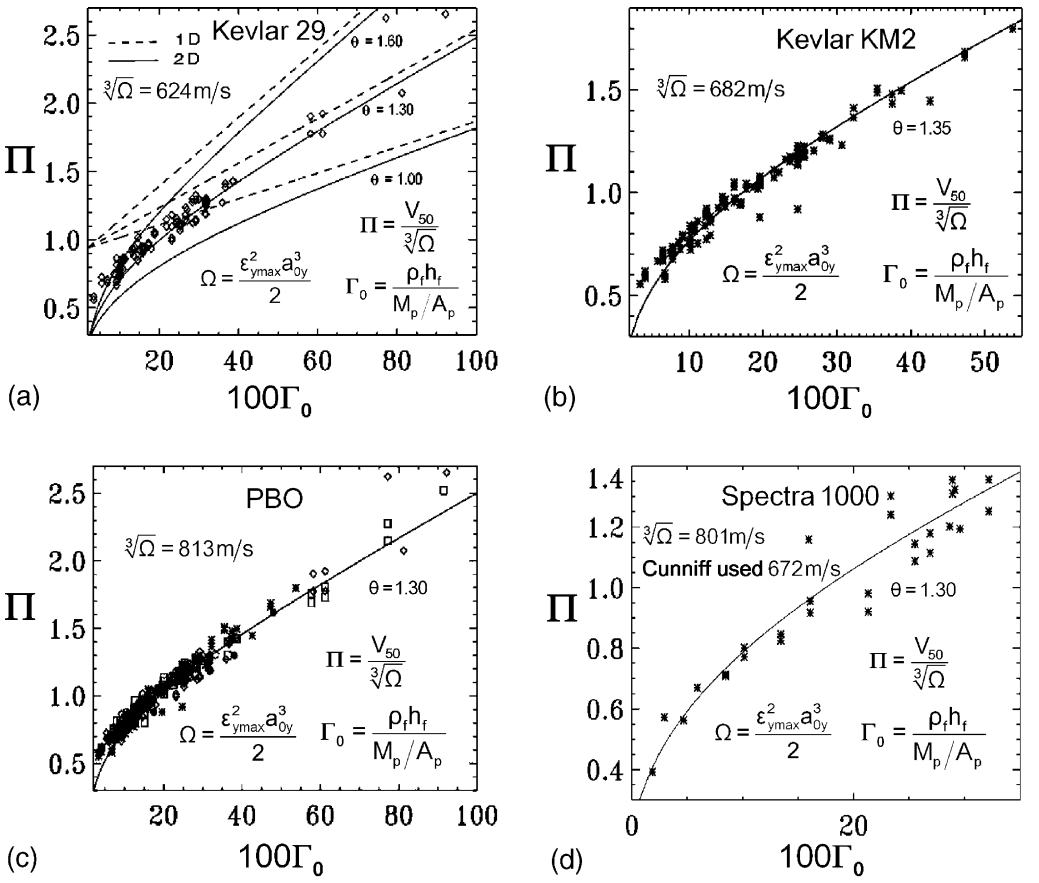

Fig. 5. V_{50} data for (a) Kevlar® 29, (b) Kevlar® KM2, (c) PBO, and (d) Spectra® 1000 multi-ply fabric systems plotted on dimensionless Π versus Γ_0 coordinates. Data are taken from figures in Cunniff (1999c), and normalized according to his fiber property values. Solid lines are 2D model theoretical predictions, Eq. (213), using the effective impact diameter, $D_{p\theta} = \theta D_p$ where θ values are shown. The effect of varying the adjustable parameter, θ, is shown in (a), which also shows results from the 1D model (dashed lines) where $K_{max} = 1$.

in the sudden momentum transfer, $(\theta - 1)D_p$, about 30%, is typically far less in fact than the thickness of the fabric systems tested in Fig. 5.

Unless θ is chosen to be about 1.3, even the 1D model prediction ends up below the data at higher values of the areal density ratio, Γ_0, as seen in Fig. 5a. This is very strong evidence that the role of θ is as stated. In 1D, $K_{max} = 1$ (see Fig. 4) and thus, the explanation must be that a larger effective area of momentum transfer than A_p, i.e., $\theta^2 A_p = 1.69 A_p$, must be involved in the impact to slow the projectile. As we see shortly, the number of fabric plies is of order 20–40, so a wrap-around and spreading effect to fabric layers underneath is the likely cause.

Walker (1999, 2001) developed a membrane model that also fit Kevlar® 29 V_{50} data from Cunniff (1999c) quite well. Similar to our θ, Walker had a parameter, $\beta = 1.6$. This amounts to an impact area inflation factor of $\beta^2 = 2.56$, whereas we have $\theta^2 \approx 1.69$. Walker's model did not account for the tension wave induced flow of membrane material towards the impact zone, so it gave very low membrane deflection angles, γ, certainly a main factor in the difference.

It is startling that the agreement in Fig. 5 a–d is so good given the many simplifying assumptions in the model and the fact that the fabric systems are biaxial and have many, relatively independent plies, whereas our membrane model has one ply that is isotropic in plane. Evidently the increased dimensionality of the fabric relative to a 1D model with right angle, crossing yarns, is the dominating aspect. Furthermore, structural details of the fabrics, such as yarn spacing, yarn denier, yarn crimp, yarn slippage, ply spacing, yarn transverse compliance, etc., were not represented in the membrane model, and for these standardized RCC projectiles seem not to be important. This is not to say that these factors are unimportant for other projectiles with sharper tips (conical, ogive, spherical) as they may strongly influence the results, as discussed shortly.

We note, in Fig. 5, that values of $\Gamma_0 > 0.2$ typically correspond to the fabric depth being greater than the projectile length. While the basic information is not provided in Cunniff (1999c), the value $\Gamma_0 = 0.2$ might correspond to say 25 or 30 plies of fabric made from 1000 denier yarns and impacted by a 16 grain (1 g) flat-nosed, cylindrical (RCC) steel projectile with a diameter of 0.55 cm and length to diameter ratio of unity. Even if highly compressed with no voids, Eq. (218) indicates that the depth, h_f, of Kevlar 29 would be about the same as that of the projectile, and as a loose multi-ply fabric, the depth would be 2–3 cm.

Note from Eq. (217) that the stopping distance δ_{p0} in this 2D example is about 0.5 cm, whereas in 1D, using Eq. (189) with $\theta^2\Gamma_0$ replacing Γ_0 and a_{0y} replacing a_0, it is about three times that value. These values might be reasonable for a highly compacted Kevlar panel but not a multi-ply fabric as the predicted stopping distance is far less than the multi-ply fabric depth. Again this begs the question as to why the single membrane model should work so well in Fig. 5, when ply failures are likely to be sequential and rather decoupled as Cunniff (1999a) suggests.

6.3. Model predictions for residual velocity after penetration compared to Cunniff's data

Fig. 6 shows a plot of residual velocity, V_{res}, versus striking velocity, V_p, calculated from our 2D membrane model, as described in Section 4.6. The solid lines to the right of the dots also coincide with the

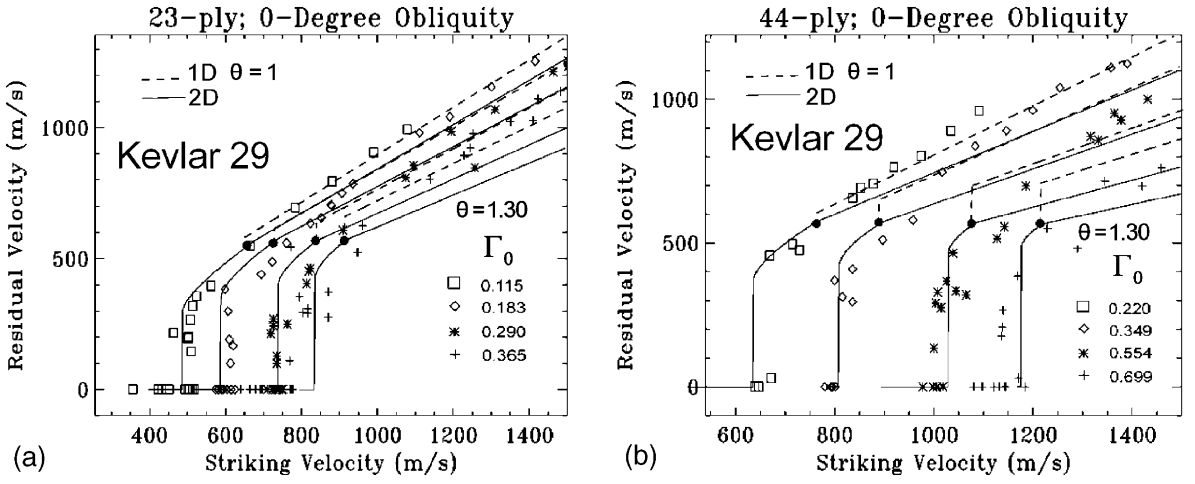

Fig. 6. Residual velocity, V_{res}, versus striking velocity, V_p, of standardized RCC projectiles into Kevlar® 29 fabric systems, (a) 23-ply and (b) 44-ply, taken from Cunniff (1999b). Areal density ratios, Γ_0, correspond to 2, 4, 16 and 64 grain RCC steel projectiles believed used in the experiments. Solid lines are based on V_{50} versus Γ_0 values from Fig. 5(a) where $\theta = 1.30$. Lines to the right of the solid dots are also the 1D solution as are the dashed lines but using $\theta = 1$ for these higher velocities implying a much smaller fabric patch area, A_p, in momentum transfer.

1D solution. Again this data is for 23-ply and 44-ply fabric systems of Kevlar 29 taken from figures in Cunniff (1999b). Unfortunately Cunniff did not provide areal density values for the fabrics, and the projectiles were not specifically identified but they are believed to have been steel RCC projectiles in the variations 2, 4, 16 and 64 grains. Based on this hypothesis and data in Fig. 5, the Γ_0 values are believed reasonable.

Within the data variability in Fig. 6, the model is consistent across this wide range of Γ_0 and gives good agreement. The most noticeable disagreement is with the 44-ply fabrics with the smallest projectiles (highest Γ_0 values). The predicted residual velocities are increasingly lower than the actual ones, as the striking velocities increase to well above the V_{50} limit. In terms of the model, this is understandable upon noting that the sequential failure of the plies will cause small $\psi_{\max}$ values for each ply compared to a single thick membrane with the same overall V_{50} so the energy absorbed per ply may be less. For the 1D model the residual velocity is simply $V_{\text{res}} = V_{\text{p}}/(1 + \theta^2\Gamma_0)$ assuming the projectile instantaneously severs a plug of the multi-ply fabric and the velocity decrease is due to momentum transfer alone. The dashed lines for 1D show the effect at higher impact velocities of taking $\theta = 1$. The data suggest that θ must decrease with increasing velocity; that is, the overall cut fabric plug size in momentum transfer decreases.

6.4. Momentum transfer consistency

In the case of a 1D tape of diameter D_{p} (2 spokes), it is possible to do a momentum transfer analysis, beginning with a square projectile with a chisel tip (with slope exceeding γ_{p0} on impact) spanning across the tape, and comparing it to that for a square-faced projectile of the same width, D_{p}. The idea is to show, in the chisel tip case, that by the time the transverse wave spans distance D_{p}, thus covering the same tape area as the blunt square tip, the projectile velocities are about the same. In the case of the chisel tip, the results in Section 4.2 can be used to show that the chisel projectile velocity becomes

$$\hat{V}_{\text{p0}} = V_{\text{p}} \exp(-\Gamma_0) = V_{\text{p}}/(1 + \Gamma_0 + \Gamma_0^2/2 + \cdots) \approx V_{\text{p}}/(1 + \Gamma_0) \tag{219}$$

The last expression is indeed our assumption, Eq. (163). The relative error is of order $\Gamma_0^2/2$, and thus, even for the large value $\Gamma_0 = 0.3$ (typical of 20 or 30 plies of fabric in body armor) the two values only differ by about 5%, and for $\Gamma_0 = 0.2$ the difference is about 2%. Thus, starting as a sharp wedge, once the wave spans the diameter D_{p} the projectile velocity will be about the same as if the impact were from a square blunt projectile of diameter, D_{p}. This is a strong consistency check for our model and indicates that the adaptation of constant velocity relationships to the case of projectile deceleration is very accurate unless Γ_0 is very large. In the latter case the fabric system will be much thicker than the projectile, contrary to the membrane assumption.

6.5. Energy distribution and absorption upon impact and potential thermal effects ($V_p < V_{50}$)

When a projectile suddenly decelerates upon impact, it loses kinetic energy and the question arises as to how this energy becomes distributed in the membrane cone and implosion wave area in terms of strain energy, kinetic energy, and energy dissipated as heat into the membrane (assuming negligible deformation of the projectile itself). In the above, ideal case of the square chisel-nosed projectile impacting a tape, we can account for this energy up to the time, t_{p}, when the triangle wave has expanded to width, D_{p}, the effective shadow cast by the projectile on the tape. The lost projectile kinetic energy by this time is distributed about half as kinetic energy of the suddenly accelerated square tape patch of area D_{p}^2 traveling in front of the projectile, and about half as the sum of strain energy plus kinetic energy in the propagating radial implosion wave, the last two being approximately equal in the sum.

In the case of a blunt-nosed square projectile, this implosion wave does not have time to grow to the same extent as in the chisel nose in the time it takes for the projectile velocity to drop from V_p to V_{p0}, so in the blunt-nosed case significant temperature changes must locally occur in the impacted membrane material as some projectile kinetic energy is converted to heat. This is important in materials such as polyethylene-based Spectra®, which have a relatively low melting temperature. It can be shown that local production of heat from the lost energy is approximately

$$\Xi_{\text{heat}} \approx (1/2)V_p^2(1-\lambda)/(1+\theta^2\Gamma_0) \tag{220}$$

per unit mass of fabric material in the impact area, where λ is a parameter close to zero in the case of extremely blunt impact, $h_f/V_p \ll D_p/c_{p0}$.

Since V_{50} velocities for fabric systems range over 300–1100 m/s over areal density ratios, Γ_0, ranging over 0.05–0.4, the kinetic energies per unit mass of fabric in the impact area, available to convert to heat following Eq. (220), may be in the range 45–600 kJ if $\lambda = 0$, and perhaps half of this value (i.e., for $\lambda = 1/2$). Mean specific heats of polymeric materials used in ballistic protection are of order 1.5–2.0 kJ/(kg K) so local temperature rises of order 25–400 K are possible if $\lambda = 0$, but for a more likely $\lambda = 1/2$ they would be 12–200 K. Thus, in view of the fact that V_{50} tends to rise with Γ_0, certain fabric materials that perform well for small Γ_0 (i.e., single ply performance where V_{50} velocities are lower) may be susceptible to thermal softening and weakening as Γ_0 increases.

In generating Fig. 5d for Spectra® 1000 fabric as in Fig. 5 a–c for the other materials, Cunniff (1999c) found that Spectra® based material data fell short of the empirical curve for the other materials unless their yarn strengths were discounted about 20%. The effect seemed to worsen as Γ_0 increased, and he suggested thermal affects as being a likely cause. Our analysis supports this contention. Indeed post mortem studies of the impact of Spectra based armor materials, which have higher values of Γ_0, reportedly show effects of local melting.

We note also that in simulations of fabric impact, oscillations and ringing are a major problem often requiring artificial introduction of viscosity of some form as in Cunniff and Ting (1999) and Johnson et al. (1999). The latter authors were uncomfortable with this viscosity introduction, mentioning its lack of physical basis. We believe this high amplitude ringing is the equivalent of the heating discussed here, and is a fundamental aspect of the problem.

6.6. Membrane impact by projectiles with paraboloid or spherical shaped noses

The above analysis was performed for flat-nosed RCC cylinders, but the question arises as to how to treat impact from other axisymmetric nose shapes, such as paraboloid, spherical, ogive or conical shapes. The latter two are problematic as the contact area is nominally zero, but in practice they would be blunted by a hard strike face. The key is to calculate an effective impact zone radius, $r_p^{\text{eff}} = D_p^{\text{eff}}/2$. Using $y = (\widehat{r}_p/2)(r/\widehat{r}_p)^2$ for a paraboloid with local tip radius, $\widehat{r}_p$, an estimate is to solve $dy/dr = r/\widehat{r}_p = \gamma_{p0}$ where $\gamma_{p0} = \{2V_p/[a_0(1+\Gamma_0)]\}^{1/3}$ is the cone angle on impact by Eqs. (145) and (163). This yields

$$r_p^{\text{eff}} = \widehat{r}_p\{2V_p/[a_0(1+\Gamma_0)]\}^{1/3} \approx \widehat{r}_p(2V_p/a_0)^{1/3} \tag{221}$$

where we have neglected $(1+\Gamma_0)^{1/3} \approx 1+\Gamma_0/3$ as negligible up to the order of the approximation. Thus for $V_p \approx 600$ m/s and $a_0 \approx 8000$ m/s the effective radius is $r_p^{\text{eff}} = \widehat{r}_p\{0.15\}^{1/3} \approx 0.531\widehat{r}_p$, or about half the radius of curvature. Repeating the calculation for a spherical projectile of radius $\widehat{r}_p$, and assuming $\gamma_{p0} \leqslant \pi/6$, the result will be approximately the same. We also expect the need for an adjustable factor $\widehat{\theta}$. Compared to a blunt cylindrical projectile, such nose shapes amount to an effective decrease in Γ_0 by a factor of about 4, and by Fig. 5 the predicted decrease in the V_{50} velocity of a fabric system would be

substantial. The shape of sharp impactors on fibrous composites remains an active research area, e.g., Ben-Dor et al. (2002) and Wen (2000).

7. Conclusions

Many results and formulas were developed in this paper, such as distance required to stop the projectile, residual velocity after penetration, and angle of membrane deflection versus impact velocity, to name a few. As was pointed out, the membrane model here has a single layer, whereas fabric systems typically consist of many identical plies ($\Gamma_0 = 0.2$ may correspond to about 25 plies) with a ply spacing of order 1 mm. Despite these complications, the model works extremely well, as Figs. 5 and 6 indicate. Nevertheless, sequential effects and the extent of ply decoupling are worthy of study, especially when plies of different types are mixed. Cunniff (1999a) has shown that the strike face layers can be replaced with low cost material compared to the underlying plies without hindering (and even improving) performance.

In Fig. 1 we presented a hypothetical, body armor with multiple layers of diverse properties, and raised many questions on its possible development. This paper lays much groundwork for modeling such behavior. Each layer must serve a purpose and as stated in Section 1 and shown again in Cunniff (1999c), simply adding a resin to the fabric system to bond fibers together and stiffen it, does not improve performance (per unit weight) except for $\Gamma_0 > 0.4$, which amounts to a fairly massive system that is unlikely to achieve the weight goals of the hypothetical system. What might seem beneficial from experience with static loading and low velocity impact may turn out to be detrimental at higher projectile velocities and misleading in guiding future research.

As it stands the model sheds light on material properties that may be necessary to greatly improve body armor performance per unit weight. The key predictor of performance is the normalizing velocity, $\sqrt[3]{\Omega}$, which can be written as

$$\sqrt[3]{\Omega} = \left(\frac{\sigma_{y\max}\varepsilon_{y\max}}{2\rho_y}\sqrt{\frac{E_y}{\rho_y}}\right)^{1/3} = \left(\frac{\varepsilon_{y\max}}{\sqrt{2}}\right)^{2/3} a_{0y} \tag{222a}$$

where all properties are basic yarn (or fiber) properties. This velocity is expressed as the cube-root of the product of the yarn elastic energy storage capacity per unit mass (a measure of toughness) and its tensile wave speed, a_{0y}. Increasing the former (as is often believed desirable) may do no good if a_{0y} is greatly reduced in the process, a situation that may occur with synthetic spider silk. Another consequence of greatly lowering a_{0y} is the need for a much larger distance to stop the projectile, as Eq. (217) shows. This would greatly increase the bulk of body armor.

We finally note that the normalizing velocity can also be written as

$$\sqrt[3]{\Omega} = \left(\frac{\sigma_{y\max}}{\sqrt{2}\rho_y}\right)^{2/3}\left(\frac{E_y}{\rho_y}\right)^{-1/6} = \left(\frac{\sigma_{y\max}}{\sqrt{2}\rho_y}\right)^{2/3} a_{0y}^{-1/3} \tag{222b}$$

suggesting that increasing the strength per unit weight of the fiber material is crucial, and if at the same time the tensile wave speed can be decreased, so much the better.

Acknowledgement

The authors would like to thank Dr. Thomas A. Godfrey of the U.S. Army's Natick Soldier Center for many helpful discussions.

References

Anderson Jr., C.E., Gooch, W.A., 2001. Numerical simulations of dynamic X-ray imaging experiments of 7.62 mm APM2 projectiles penetrating B_4C. In: Proceedings of the 19th International Symposium of Ballistics, Interlaken, Switzerland. pp. 1423–1429.

Ballistic Resistance of Body Armor, NIJ Standard-0101.04, Revision A, National Institute of Justice, June 2001.

Ben-Dor, G., Dubinsky, A., Elperin, T., 2002. A model for predicting penetration and perforation of FRP laminates by 3-D impactors. Compos. Struct. 56, 243–248.

Boyce, W.E., DiPrima, R.C., 1997. Elementary Differential Equations and Boundary Value Problems. Wiley, New York.

Cheeseman, B.A., Bogetti, T.A., 2003. Ballistic impact into fabric and compliant composite laminates. Compos. Struct. 61, 161–173.

Chocron-Benloulo, I.S., Rodriguez, J., Sanchez-Galvez, V., 1997. A simple analytical model to simulate textile fabric ballistic impact behavior. Text. Res. J. 67, 34–41.

Cole, J.D., Dougherty, C.B., Huth, J.H., 1953. Constant-strain waves in strings. ASME J. Appl. Mech. 20, 519–522.

Craggs, J.W., 1954. Wave motion in plastic–elastic strings. J. Mech. Phys. Solids 2, 286–295.

Cristescu, N., 1954. Loading and unloading waves in an elastic or plastic flexible fiber. Prikl. Mat. Mekh. 18, 257–264 (in Russian).

Cunniff, P.M., 1992. An analysis of the system effects in woven fabrics under ballisitic impact. Text. Res. J. 56, 45–60.

Cunniff, P.M., 1996. A semi-empirical model for the ballistic impact performance of textile-based personnel armor. Text. Res. J. 56, 45–60.

Cunniff, P.M., 1999a. Decoupled response of textile body armor. In: Proceedings of the 18th International Symposium of Ballistics, San Antonio, Texas. pp. 814–821.

Cunniff, P.M., 1999b. V_s–V_r relationships in textile system impact. In: Proceedings of the 18th International Symposium of Ballistics, San Antonio, Texas.

Cunniff, P.M., 1999c. Dimensional parameters for optimization of textile-based body armor systems. In: Proceedings of the 18th International Symposium of Ballistics, San Antonio, Texas. pp. 1303–1310.

Cunniff, P.M., Ting, J., 1999. Development of a numerical model to characterize the ballistic behavior of fabrics. In: Proceedings of the 18th International Symposium of Ballistics, San Antonio, Texas. pp. 814–821.

Fatt, M.S.H., Lin, C., Revilock Jr., D.M., Hopkins, D.A., 2003. Ballistic impact of GLARE fiber–metal laminates. Compos. Struct. 61, 73–88.

Galin, M.P., 1949. Impact on a flexible plate. Sbornik Statei Instituta Mekhaniki.

Graff, K.F., 1991. Wave Motion in Elastic Solids. Dover Publications, New York (originally Oxford Clarendon University Press, 1975).

Grigor'ev, V.S., 1949. Study of the tension and elongation of a warp thread in the KR-46 textile machine. Ph.D. Thesis presented to the Moscow Textile Institute.

Grigoryan, D.M., 1949. Normal impact on an unbounded thin diaphragm. PPM 13 (3), 277–284.

Johnson, G.R., Beissel, S.R., Cunniff, P.M., 1999. A computational model for fabrics subjected to ballistic impact. In: Proceedings of the 18th International Symposium of Ballistics, San Antonio, Texas. pp. 962–969.

Keefe, M., Duan, Y., Bogetti, T., Cheeseman, B., 2002. Modeling the impact behavior of high-strength fabric structure. Fiber Society Lecture, Fall Meeting, Natick MA.

Lee, S.-W.R, Sun, C.T., 1993. Dynamic penetration of graphite/epoxy laminates impacted by a blunt-ended projectile. Compos. Sci. Technol. 49, 368–380.

Lim, C.T., Shim, V.P.W., Ng, Y.H., 2003. Finite-element modeling of the ballistic impact of fabric armor. Int. J. Impact Eng. 28, 13–31.

Maheux, C.R., 1957. Dynamics of body armor materials under high speed impact. Part I: Transient deformation, rate of deformation and energy absorption in single and multilayer armor panels. US Army Chemical Center Report, CWLR 2141, Edgewood, MD.

Mehta, P.K., Davids, N., 1966. A direct numerical analysis method for cylindrical and spherical elastic waves. Am. Inst. Aeronaut. Astronaut. J. 4, 112–117.

Montgomery, T.G., 1980. The Effects of Geometric shape of an impacting projectile on the energy absorption process in woven fabric systems. Ph.D. Thesis, North Carolina State University.

Moroz, G.S., 1956. Transient stages in the motion of a flexible fiber of finite length upon normal impact. Prikl. Mat. Mekh. 20.

Morrison, C., 1984. The mechanical response of an aramid textile yarn to ballistic impact. Ph.D. Thesis, University of Surrey.

Pavlenko, A.A., 1952. Direct impact of a body of revolution of a given profile on a flexible plate. Ph.D. Thesis presented to the Scientific Research Institute for Mechanics and Mathematics of Moscow University.

Prevorsek, D.C., Chin, H.B., Kwon, Y.D., 1991. Strain rate effects in ultrasonic polyethylene fibers and composites. J. Appl. Poly. Sci.: Appl. Poly. Symp. 47, 45–66.

Prosser, R.A., 1988. Penetration of nylon ballistic panels by fragment-simulating projectiles. Part I: A linear approximation to the relationship between the square of the V_{50} or V_c striking velocity and the number of layers of cloth in the ballistic panel. Text. Res. J. 48, 61–85.

Rakhmatulin, Kh.A., 1945. Oblique impact at a large velocity on a flexible fiber in the presence of friction. Prikl. Mat. Mekh. 9, 449–462 (in Russian).
Rakhmatulin, Kh.A., 1947. Impact on a flexible fiber. Prikl. Mat. Mekh. 11, 379–382 (in Russian).
Rakhmatulin, Kh.A., 1951. Normal impact at a varying velocity on a flexible fiber. Uchenye Zapiski Moskovosk gos. Univ. 4, 154 (in Russian).
Rakhmatulin, Kh.A., 1952. Normal impact on a flexible fiber by a body of given shape. Prikl. Mat. Mekh. 16, 23–24 (in Russian).
Rakhmatulin, Kh.A., Dem'yanov, Yu.A., 1961. Strength Under High Transient Loads. pp. 94–152 (English translation, Israel Program for Scientific Translations, 1966).
Ringleb, F.O., 1957. Motion and stress of an elastic cable due to impact. J. Appl. Mech. 24, 417–425.
Roylance, D., 1973. Wave propagation in a viscoelastic fiber subjected to transverse impact. ASME J. Appl. Mech. 40, 143–148.
Roylance, D., Hammas, P., Ting, J., Chi, H., Scott, B., 1995. Numerical modeling of fabric impact. In: Proceedings of the ASME National Meeting, AD-Vol. 48, San Francisco, 1995.
Roylance, D., Wang, S.S., 1980. Penetration mechanics of textile structures. In: Laible, R.C. (Ed.), Ballistic Materials and Penetration Mechanics. Elsevier, pp. 273–293 (Chapter 12).
Roylance, D.K., Wilde, A.F., Tocci, C., 1973. Ballistic impact of textile structures. Text. Res. J. 43, 34–41.
Ryabova, E.V., 1953. Normal impact at a varying velocity on a flexible fiber. Vestnik Moskovosk Univ. 10, 85–91 (in Russian).
Scott, B.R., 1999. The penetration of compliant laminates by compact projectiles. In: Proceedings of the 18th International Symposium of Ballistics, San Antonio, Texas. pp. 1181–1191.
Shim, V.P., Tan, V.B.C., Tay, T.E., 1995. Modeling deformation and damage characteristics of woven fabrics under small projectile impact. Int. J. Impact Eng. 16, 585–605.
Simons, J.W., Erlich, D.C., Shockey, D.A., 2001. Finite element design model for ballistic response of woven fabrics. In: Proceedings of the 19th International Symposium of Ballistics, Interlaken, Switzerland. pp. 1415–1422.
Smith, J.C., Blandford, J.M., Schiefer, H.F., 1960. Stress–strain relationships in yarns subjected to rapid impact loading. Part VI: Velocities of strain waves resulting from impact. Text. Res. J. 30, 752–760.
Smith, J.C., Fenstermaker, C.A., Shouse, P.J., 1963. Stress–strain relationships in yarns subjected to rapid impact loading. Part X: Stress–strain curves obtained by impacts from rifle bullets. Text. Res. J. 33, 919–934.
Smith, J.C., McCrackin, F.L., Schiefer, H.F., 1958. Stress–strain relationships in yarns subjected to rapid impact loading. Part V: Wave propagation in long textile yarns impacted transversely. Text. Res. J. 28, 288–302.
Starratt, D., Sanders, T., Cepus, T., Poursartip, A., Vaziri, R., 2000. An efficient method of continuous measurement of projectile motion in ballistic impact experiments. Int. J. Impact Eng. 24, 155–170.
Starratt, D., Pageau, G., Vaziri, R., Poursartip, A., 1999. An instrumented experimental study of the ballistic impact response of Kevlar fabric. Proceedings of the 18th International Symposium of Ballistics, San Antonio, Texas. pp. 1208–1215.
Taylor, G.I., 1942. The plastic wave in a wire extended by an impact load. In: Mechanics of Solids Paper 32. In: The Scientific Papers of Sir G.I. Taylor, vol. 1. Cambridge University Press. 1956.
Ting, J., Roylance, D., Chi, C.H., Chitrangad, B., 1993. Numerical modeling of fabric panel response to ballisitic impact. In: Proceedings of 25th SAMPE Technical Conference.
Vinson, J.R., Walker, J.M., 1997. Ballistic impact of thin-walled composite structures. Am. Inst. Aeronaut. Astronaut. J. 35, 875–878.
Vinson, J.R., Zukas, J.A., 1975. On the ballistic impact of textile armor. ASME J. Appl. Mech. 42, 263–268.
von Karmann, T., 1942. On the propagation of plastic deformation in solids. National Defense Research Council Report A.33.
Walker, J.D., 2001. Ballistic limits of fabrics with resin. In: Proceedings of the 19th International Symposium of Ballistics, Interlaken, Switzerland. pp. 1409–1414.
Walker, J.D., 1999. Constitutive model for fabrics with explicit static solution and ballistic limit. In: Proceedings of the 18th International Symposium of Ballistics, San Antonio, Texas. pp. 1231–1239.
Wen, H.M., 2000. Predicting the penetration and performance of FRP laminates struck normally by projectiles with different nose shapes. Compos. Struct. 49, 321–329.
Wilde, A.F., Roylance, D.K., Rogers, J.M., 1973. Photographic investigation of high-speed missile impact upon nylon fabric. Part I: Energy absorption and cone radial velocity in fabric. Text. Res. J. 43, 753–761.
Wilde, A.F., Roylance, D.K., Rogers, J.M., 1974. Photographic investigation of high-speed missile impact upon nylon fabric. Part II: Retarding force on missile and transverse critical velocity. Text. Res. J. 44, 772–778.
Zverev, I.N., 1949. Some problems concerning wave propagation upon impact. Ph.D. Thesis, Scientific Research Institute for Mechanics and Mathematics of Moscow University.